Grid-Adapted FUN3D Computations for the Second High Lift Prediction Workshop (Invited)

E. M. Lee-Rausch*, C. L. Rumsey† and M. A. Park‡
NASA Langley Research Center, Hampton VA 23681-2199

Contributions of the unstructured Reynolds-averaged Navier-Stokes code FUN3D to the 2nd AIAA CFD High Lift Prediction Workshop are described, and detailed comparisons are made with experimental data. Using workshop-supplied grids, results for the clean wing configuration are compared with results from the structured code CFL3D Using the same turbulence model, both codes compare reasonably well in terms of total forces and moments, and the maximum lift is similarly over-predicted for both codes compared to experiment. By including more representative geometry features such as slat and flap brackets and slat pressure tube bundles, FUN3D captures the general effects of the Reynolds number variation, but under-predicts maximum lift on workshop-supplied grids in comparison with the experimental data, due to excessive separation. However, when output-based, off-body grid adaptation in FUN3D is employed, results improve considerably. In particular, when the geometry includes both brackets and the pressure tube bundles, grid adaptation results in a more accurate prediction of lift near stall in comparison with the wind-tunnel data. Furthermore, a rotation-corrected turbulence model shows improved pressure predictions on the outboard span when using adapted grids.

I. Introduction

The 2nd AIAA CFD High Lift Prediction Workshop (HiLiftPW-2) was held at the 31st Applied Aerodynamics Summer Conference in San Diego, California, in June 2013.[a] As with the first workshop,[1] the main objective of HiLiftPW-2 was to assess the numerical prediction capability (meshing, numerics, turbulence modeling, high-performance computing requirements, etc.) of current-generation CFD technology (codes) for swept, medium-to-high-aspect ratio wings for landing/take-off (high-lift) configurations. Additional goals of the workshop included the following: develop practical modeling guidelines for CFD prediction of high-lift flow fields, determine the elements of high-lift flow physics that are critical for modeling to enable the development of more accurate prediction methods and tools, and enhance CFD prediction capability for practical high-lift aerodynamic design and optimization. The workshop analyzed the flow over the DLR-F11 model in landing condition. Twenty-six participants submitted a total of 48 data sets of CFD results on a variety on grid systems (both structured and unstructured). An overview and summary of the workshop is given by Rumsey and Slotnick.[2] Many workshop participants have summarized individual submissions and provided additional analysis and computations.[3–11]

In the workshop, CFD codes were reasonably consistent with each other at lower angles of attack and exhibited larger variations at high angles of attack near maximum lift. The importance of including slat and flap brackets when comparing with experiment was established, and there was also evidence that the presence of pressure tube bundles lying along-side the slat brackets significantly influenced the flowfield in the experiment near maximum lift. In other words, the prediction of $C_{L,max}$ for realistic high-lift configurations like the DLR-F11 continues to be a significant challenge for CFD. Many factors are necessary for a CFD calculation to successfully predict such a flow field, including geometric fidelity (e.g., including all relevant geometry such as support brackets and pressure tube bundles), sufficient grid resolution in regions where it is needed and accurate turbulence modeling.

*Research Engineer, Computational AeroSciences Branch, E.Lee-Rausch@nasa.gov. Senior Member AIAA.
†Senior Research Scientist, Computational AeroSciences Branch, C.L.Rumsey@nasa.gov. Fellow AIAA.
‡Research Scientist, Computational AeroSciences Branch, M.A.Park@nasa.gov. Senior Member AIAA.
[a]Data available online at http://hiliftpw.larc.nasa.gov [retrieved 2/10/2014].

In the current paper, the basic contributions of FUN3D and CFL3D to HiLiftPW-2 are described. However, the basic results, which were very similar to other workshop contributions, do not add any significant insights beyond what was learned at the workshop collectively. Therefore, this paper goes further and investigates the effect of output-based, off-body grid adaptation applied to the DLR-F11, particularly near $C_{L,max}$. This technology is believed to be a key enabler for improved CFD predictions. The additional computations also explore the influence of a turbulence model rotation correction.

The paper is organized as follows. First, the CFD codes are described. Then, output-based grid adaptation (as implemented in FUN3D) is outlined. The HiLiftPW-2 cases are summarized in Section V, and results are included in Section VI. The results are divided into two sub-sections. Section A includes a grid convergence study, a Reynolds number effect study and a full configuration study on workshop-supplied grids. Section B includes grid-adapted results using FUN3D on the configuration with successively increasing geometric fidelity, including clean wing, wing with brackets and wing with brackets and pressure tube bundles. This work shows the importance of grid adaptation for predicting important features of high-lift flow fields, ultimately leading to better and more consistent prediction of $C_{L,max}$.

II. CFL3D Flow Solver

CFL3D[12] is a structured-grid upwind multi-zone CFD code that solves the generalized thin-layer or full Navier-Stokes equations. In the current study, the full viscous terms are used for all computations. CFL3D can use point-matched, patched, or overset grids and employs local time-step scaling, grid sequencing and multigrid to accelerate convergence to steady state. CFL3D is a cell-centered finite-volume method. It uses third-order upwind-biased spatial differencing on the convective and pressure terms, and second-order differencing on the viscous terms; it is globally second-order accurate. Roe's flux difference-splitting method[13] is used to obtain fluxes at the cell faces. The solution is advanced in time with an implicit approximate factorization method. For each loosely coupled iteration, the mean flow equations are advanced in time with the eddy-viscosity fixed; then the turbulence model is advanced in time with the mean flow solution fixed. Several turbulence models are available in the code, including the one-equation model of Spalart-Allmaras[14] (SA), the two-equation shear stress transport (SST) model of Menter,[15] and the four-equation γ-Re_θ SST transition model of Langtry-Menter.[16] However, in studies for the high-Reynolds number clean wing case (not shown here), the choice of turbulence model was seen to have little influence; so results will only be shown for SA.

III. FUN3D Flow Solver

FUN3D[17–19] is a finite-volume Navier-Stokes solver in which the flow variables are stored at the vertices or nodes of the mesh. FUN3D solves the equations on mixed element grids, including tetrahedra, pyramids, prisms and hexahedra. The code also has a two-dimensional path for triangular and quadrilateral grids. At interfaces between neighboring control volumes, the inviscid fluxes are computed using an approximate Riemann solver based on the values on either side of the interface. Several convective flux schemes are available in FUN3D. The most common scheme for subsonic and transonic flows is Roe's flux difference splitting,[13] which is used in the current study. For second-order accuracy, interface values are obtained by extrapolation of the control volume centroidal values, based on gradients computed at the mesh vertices using an unweighted least-squares technique. Several reconstruction limiters are available in FUN3D, but none were used in this study.

For tetrahedral meshes, the full viscous fluxes are discretized using a finite-volume formulation in which the required velocity gradients on the dual faces are computed using the Green-Gauss theorem. On tetrahedral meshes this is equivalent to a Galerkin type approximation. For non-tetrahedral meshes, the same Green-Gauss approach can lead to odd-even decoupling. A pure edge-based approach can be used to circumvent the odd-even decoupling issue, but yields only approximate viscous terms. Thus for non-tetrahedral meshes, the edge-based gradients are combined with Green-Gauss gradients, which improves the h-ellipticity of the operator, and allows the complete viscous stresses to be evaluated.[20] This formulation results in a discretization of the full Navier-Stokes equations.

The solution at each time-step is updated with a backwards Euler time-integration scheme. At each time step, the linear system of equations is approximately solved with either a multi-color point-implicit procedure or an implicit-line relaxation scheme.[21] Local time-step scaling is employed to accelerate convergence to

steady state. For turbulent flows, several models are available within FUN3D. In the current study, the loosely coupled SA model[14] and its rotation variant SAR[22] are used.

IV. Output-Based Adaptation

Typically, feature-based adaption increases mesh resolution where a variable that identifies a feature of the solution is larger than average. An alternative method to feature-based adaptation is an output-based (adjoint) method that constructs an error estimate to improve the calculation of a specified engineering output functional (e.g., lift, drag). The discrete adjoint formulation of the governing flow equations has been developed to provide sensitivity derivatives of output functionals to design variables. These adjoint equations can also provide a linear relationship between a distribution of local truncation error estimates and a specified output function. The output-based adaption method therefore requires not only the solution of the governing flow equations but also the solution of the corresponding discrete adjoint equations.[19,23,24]

The linear adjoint equations are solved in FUN3D with a dual-consistent time-marching method.[21] The flowfield adjoint equations are solved in an exact dual manner, which ultimately guarantees an asymptotic convergence rate that is identical to the primal problem and costate variables that are discretely adjoint at every iteration of the solution process. To improve adjoint iterative convergence and stability, a generalized conjugate residual (GCR) scheme[25] is used with the standard multi-color point-implicit procedure as search directions.

The current output-based adaption method is based on the 2D output-based error estimation and adaptation scheme developed by Venditti,[26] which utilizes an embedded grid. This method has been implemented in 3D[27] within a parallel[28] framework for use with FUN3D flow and discrete adjoint solutions. The embedded grid required for the Venditti error estimator can be prohibitively large (eight times original grid) for 3D problems, which can limit the problem size of the output adaptive method. To avoid this limitation, a single-grid error estimation procedure has been developed and compared to the embedded-grid procedure for Euler problems[24] and turbulent simulations.[29] The current work utilizes the single grid error estimator.

Venditti[26] developed a procedure to calculate a new grid spacing request from the adaptive indicator and a user specified error tolerance. The anisotropy of mesh elements is based on the Mach Hessian (M), where the element size in the smallest spacing direction is dictated by the output-based new grid spacing request.[26] The anisotropic spacing request is specified by scaling the metric, M, to match the smallest spacing direction of the output-based request. A constant-complexity scaling[30] can optionally be applied to M to allow the user to directly specify the size of the adapted grid. This size can be set to obtain an optimal grid that is computable with available resources. In this study, the user specified error tolerance is set to half the total remaining error estimate in lift-to-drag ratio for each adaptation except where noted.

In this study, the parallel grid mechanics described by Park and Darmofal[24,31] are used to modify the grid. The adaptation mechanics have only been implemented for the tetrahedral element type. The local elemental operators of node insertion, node movement, element swap, and element collapse are utilized to iteratively drive the edge lengths to unity in M. The grid adaptation mechanics suffer from robustness problems when performing highly anisotropic adaptation near curved boundaries. Also, the discretization in FUN3D is more accurate for semi-structured right-angle elements in the boundary layer.[20] To address both of these issues, the near wall boundary layer grid is kept constant or frozen during the adaptation process. For this study, the grid is fixed within 0.5 millimeters (1.44×10^{-3} of the reference chord) of solid boundaries. This approach is not applicable to problems with initially under-resolved geometry or boundary layers, because that portion of the grid is held constant during the simulation. However, this approach is a powerful technique for problems with important off-body anisotropic features, i.e., vortices and wakes. Details of the frozen boundary layer adaptation technique are available in Andren and Park[32] and Park and Carlson.[33]

V. High-Lift Prediction Workshop Cases

The HiLiftPW-2 test cases were based on the European High Lift Programme (EUROLIFT) DLR-F11 high lift landing configuration which was tested in the Low Speed Wind Tunnel of Airbus in Bremen (B-LSWT) and the European Transonic Wind Tunnel (ETW) in Cologne.[34] The configuration is representative of a commercial wide-body twin-jet high-lift configuration with three continuous elements: full-span slat, main and full-span flap. Although multiple slat and flap settings were tested, the workshop test cases focused

on a landing configuration (slat angle 26.5° and flap angle 32°). The reference geometric quantities for the DLR-F11 are summarized in Table 1. For the CFD simulations, the geometry was approximated in a series of configurations that built up the model for improved geometric fidelity:

- Config 2 - wing/body/high lift (HL) system plus side-of-body (SOB) flap seal;
- Config 4 - same as Config 2 plus slat and flap support brackets;
- Config 5 - same as Config 4 plus slat pressure tube bundles

The model has 7 slat support brackets/fairings (SB1–SB7) and 5 flap support brackets/fairings (FB1–FB5). These are numbered from inboard to outboard. While the wind tunnel model was tested as a semi-span model, all the workshop test cases were specified to be run in "free-air" using a computational symmetry plane at the center line of the geometry. The experiment did not have specified transition on the model. However in the workshop, the boundary layer was to be modeled as "fully turbulent" (FT) in the CFD simulations, i.e., turbulence is modeled in all areas of the computational domain. Photographs of the model in the B-LSWT, Fig. 1, provide a view of the body and support brackets.

The model was tested at low Reynolds number ($Re_c = 1.35 \times 10^6$) in the B-LSWT as well as high Reynolds number ($Re_c = 15 \times 10^6$) in the ETW. A significant amount of high-quality surface and flowfield data are available, including data for an assessment of Reynolds number scale effects. Forces, moments and surface pressures were measured in both facilities. The total force and moment measurements include the body(fuselage) contributions. The low Reynolds number test included flowfield velocity measurements using particle image velocimetry (PIV) and oil flow visualization. Figure 1(b) shows the three PIV planes located at $\eta = 0.176, 0.700$ and 0.874. Figure 2 shows the locations and naming convention for the velocity profiles provided to the workshop. The oil visualization from the low Reynolds number experiment suggests that at stall large isolated areas of separated flow exist over the main wing behind two of the brackets (SB5 and SB6) and in front of two of the flap tracks (FB3 and FB4), which spread out laterally towards the trailing edge. Details regarding the experimental geometry, data and repeatability can be found in Rudnik et al.[34]

Table 1. Reference geometry for the DLR-F11.

Wing Reference Chord, c_{ref}	0.34709 meter
Wing Reference Area, $A/2$	0.41913 meter^2
Wing Half Span, $b/2$	1.4 meter
Aspect Ratio, AR	9.353
Quarter Chord Sweep angle	30.0°

The first required test case (Case 1) for the workshop was a high Reynolds number, grid convergence study for Config 2 at two anlges of attack: $\alpha = 7°$ and 16°. A family of three grids was required for the study with consistent levels of refinement between each grid: coarse, medium and fine. An additional extra-fine mesh solution was optional. The second required test case (Case 2) for the workshop was a Reynolds number study, which required an angle-of-attack sweep for Config 4 at two different Reynolds numbers conditions corresponding to the B-LSWT (Case 2a) and ETW (Case 2b) test conditions. Case 2 computations were performed on a set of medium-sized grids. Case 2c was an optional case at the low Reynolds number condition run with specified transition or transition prediction methods. The optional full configuration effects study (Case 3) was performed on medium-sized grids run with fully turbulent and/or with transition modeled. For Cases 1–3, workshop participants were asked to run on at least one of the grid series supplied by the HiLiftPW committee. The HiLiftPW-2 committee did not provide point-matched structured grids for Case 2. The fourth test case was a simple turbulence model verification study included to isolate potential inconsistencies in turbulence model implementations. The four test cases for the workshop are summarized here:

Case 1 : Grid convergence study (required)

DLR F11 "Config 2" - Slat 26.5°, Flap 32° (Wing/Body/HL system + SOB Flap Seal)
$M_\infty = 0.175$, free-air
$Re_c = 15.1 \times 10^6$, fully turbulent
Angles-of-attack = 7° and 16° (18.5°, 20°, 21° and 22.4° optional)
Coarse, medium, fine and extra-fine (optional)

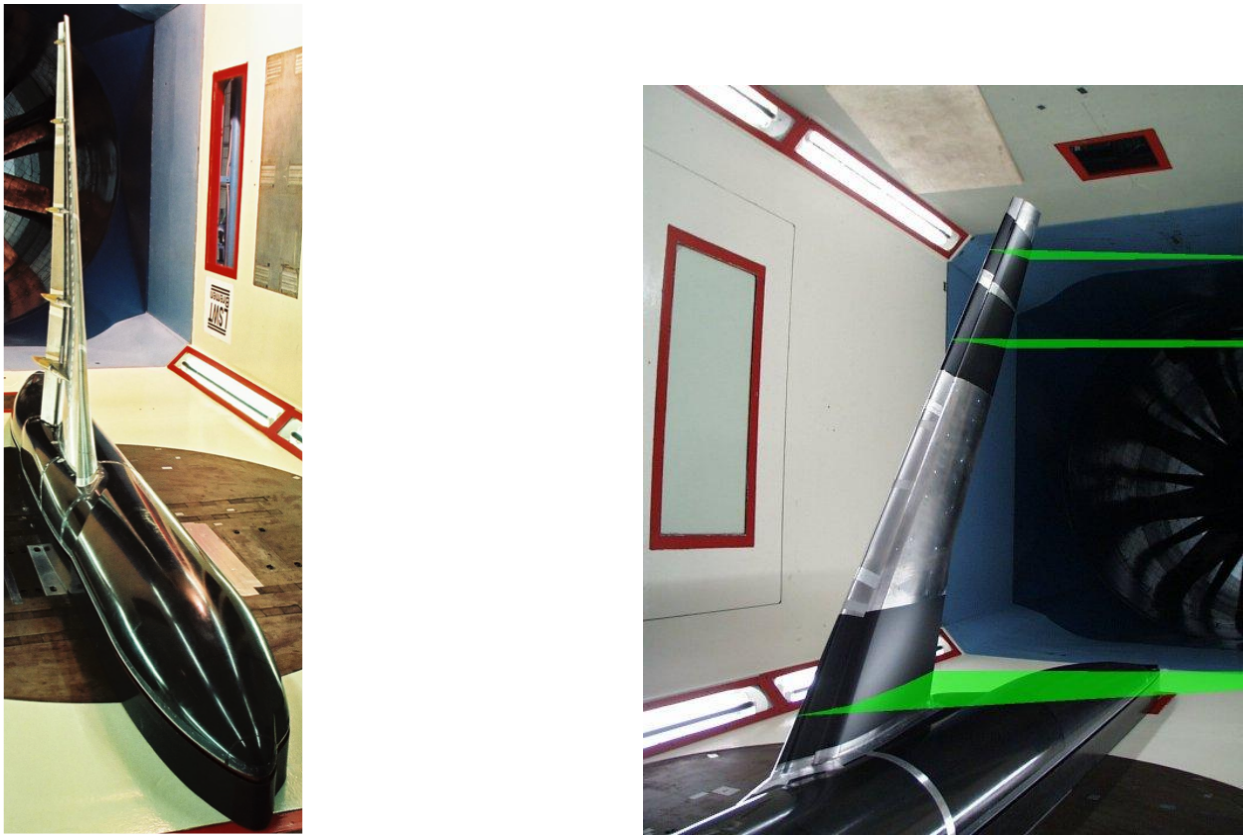

(a) Photo of model in B-LWST

(b) Location of PIV planes

Figure 1. DLR-F11 wind tunnel model.

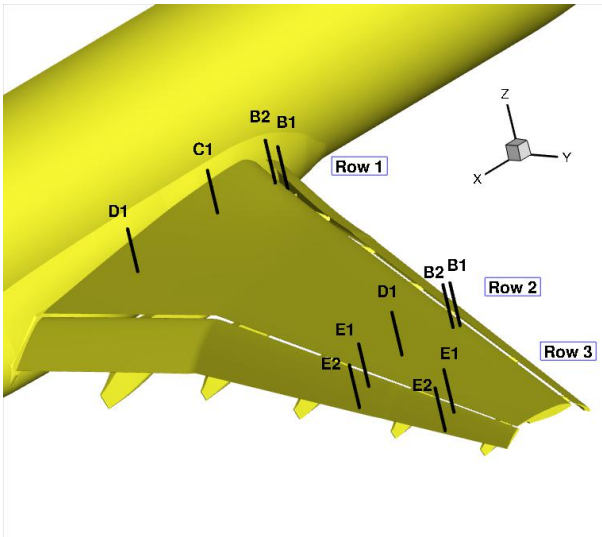

Figure 2. DLR-F11 wind tunnel model pressure tap locations.

Case 2 : Reynolds number study (required)

DLR F11 "Config 4" - Slat 26.5°, Flap 32° (Config 2 + Slat Brackets and Flap Brackets) $M_\infty = 0.175$, free-air
Angles-of-attack = 0°, 7°, 12°, 16°, 18.5°, 19°, 20° and 21° (Case 2a/c)
Angles-of-attack = 0°, 7°, 12°, 16°, 18.5°, 20°, 21° and 22.4° (Case 2b)
$Re_c = 1.35 \times 10^6$, fully turbulent (Case 2a)
$Re_c = 15.1 \times 10^6$, fully turbulent (Case 2b)
$Re_c = 1.35 \times 10^6$, specified transition and/or transition prediction methods (Case 2c optional)
Medium density mesh from Grid Convergence Study

Case 3 : Full Configuration Study (optional)

DLR F11 "Config 5" - Slat 26.5°, Flap 32° (Config 4 + Slat Pressure Tube Bundles)
$M_\infty = 0.175$, free-air
Angles-of-attack = 0°, 7°, 12°, 16°, 18.5°, 19°, 20° and 21° (Case 3a)
Angles-of-attack = 0°, 7°, 12°, 16°, 18.5°, 20°, 21° and 22.4° (Case 3b)
$Re_c = 1.35 \times 10^6$, fully turbulent and/or with transition (Case 3a)
$Re_c = 15.1 \times 10^6$, fully turbulent and/or with transition (Case 3b)
Medium density mesh from Grid Convergence Study

Case 4 : Turbulence Model Grid-Convergence Verification Study (optional)

2-D bump case from http://turbmodels.larc.nasa.gov
M = 0.2, Re = 3 million per unit length
Grid convergence study (at least 3 finest grid levels)

VI. Results

For the workshop, the required Case 1 (clean wing) was computed using both CFL3D and FUN3D, and the required Cases 2a and 2b (wing with slat and flap brackets) were computed using FUN3D. Case 4 was also computed and submitted to the workshop; CFL3D and FUN3D results can be found on the Turbulence Modeling Resource website.[b] All workshop submissions were computed with the SA model. The optional cases, Case 2c and Case 3, were not computed for the workshop. However, some full configuration (Case 3b) cases were computed after the workshop with FUN3D on workshop-supplied grids. FUN3D was also used with its adaptive-grid capability to compute Case 1, Case 2b, and Case 3b after the workshop.

The CFL3D workshop results were computed with the block-structured one-to-one grids generated by Boeing (which were only generated for the clean wing configuration). This family of grids has been denoted as grid system A for the workshop. The FUN3D workshop results were computed with the unstructured mixed-element grids generated by University of Wyoming (UWYO) and Cessna Aircraft. This family of grids has been denoted as grid system D for the workshop. The committee requested that all grids be developed according to a best-practice guideline published to the workshop website. For Case 1, the target wall spacing for the coarse, medium and fine grids was $y^+ \sim 1.0$, $y^+ \sim 2/3$ and $y^+ \sim 4/9$, respectively. For Cases 2b and 3b, the target wall spacing was $y^+ \sim 2/3$. The same mesh was used for Case 2a at the lower Reynolds number. Additional details about the gridding guidelines and specific grids are not provided here, but documentation can be found in Refs. 2 and 3 or on the HiLiftPW-2 website.[c] A comparison of grid sizes is shown in Table 2 for the workshop-supplied grids. Output-based, off-body grid adaptation was applied to the unstructured-grid solutions as described in Section IV for a selected number of configurations and angles of attack. All of the CFL3D and FUN3D runs are summarized in Table 3. The grid sizes for the final adapted grids will be discussed in subsequent sections.

Many workshop participants in HiLiftPW-1 noted a sensitivity of their solutions to the initial conditions of the computation, especially at higher angles of attack.[1] The current authors also found that initializing the computation with free-stream conditions could result in a solution with stall characteristics at lower angles of attack than a solution that was initialized from a previously converged computation at a lower angle of attack.[29] In the current computations, the fixed-grid size solutions were initialized from a previously converged computation at a lower angle of attack (when possible). This strategy was also applied to the

[b]Data available online at http://turbmodels.larc.nasa.gov/bump.html [retrieved 2/10/2014].
[c]Data available online at http://hiliftpw.larc.nasa.gov [retrieved 2/10/2014].

adapted grid results where solutions were initialized from a previously converged computation at the lower angle of attack on the final adapted grid.

Table 2. Comparison of grid sizes for workshop-supplied grids.

Grid System: Case	Coarse	Medium	Fine
A (Boeing): Case 1	11M cells	34M cells	105M cells
D (UWYO/Cessna): Case 1	10M nodes	31M nodes	76M nodes
D (UWYO/Cessna): Case 2a		42M nodes	
D (UWYO/Cessna): Case 2b		42M nodes	
D (UWYO/Cessna): Case 3b		44M nodes	

Table 3. Summary of runs.

Code/Case	Coarse	Medium	Fine
CFL3D/Case 1	A-polar	A-polar	A-polar
FUN3D/Case 1	D-polar, adapted-16°	D-polar, adapted-16°	D-polar
FUN3D/Case 2a		D-polar	
FUN3D/Case 2b		D-polar, adapted-16°,18.5°,19°,20°,21°	
FUN3D/Case 3b		D-polar, adapted-16°,18.5°,19°,20°	

A = struct. 1-to-1 A (Boeing)
D = unst. mixed D (UWYO/Cessna)
adapted = adapted grids

VI.A. Workshop Grids

VI.A.1. Grid Convergence Study (Case 1) with FUN3D and CFL3D

The effects of grid refinement were explored for Config 2 (clean wing) over a range of angles of attack: $\alpha = 7°$ – 22.4°. Figure 3 shows the total lift, drag and pitching moment polars for both CFL3D and FUN3D. The structured grid and unstructured grid results with same turbulence model (SA) compare reasonably well in forces and moment, and the trends with grid refinement are consistent. Both codes over-predict the maximum lift coefficient, $C_{L,max}$, in comparison with the experimental data. Neither predict stall on the clean wing within the angle-of-attack range explored. Both codes also over-predict the drag coefficient and predict too large a nose-down pitching moment. The over-prediction of maximum-lift, drag, and nose-down pitching moment for Case 1 is consistent with the majority of workshop submissions.[2] Eliasson and Peng have attributed part of the drag and moment disagreement between experiment and computation on the effect of half-span testing.[5]

Figure 4 shows C_L, C_D, and C_M for Case 1 as a function of $N^{-2/3}$, where N represents the number of grid points (for a node-centered scheme) or grid cells (for a cell-centered scheme). The results for all angles are summarized in Fig. 4(a) whereas the individual results for $\alpha = 7°$ and $\alpha = 16°$ are detailed in Figs. 4(b) and (c). On consistently and sufficiently refined grids that lie in the asymptotic range of grid convergence, a spatially second-order method should produce a straight line when plotted in this manner. As seen in the figure, the behaviors were not always linear, especially the FUN3D results at the higher angles of attack. Some participants noted at the workshop that the fine grid for grid system D had an incorrect minimum wall spacing and so was not of a "similar" family to the coarse and medium grids. After the workshop, the fine grid was re-generated with the correct wall spacing, and FUN3D results for Case 1 at $\alpha = 7°$ and $\alpha = 16°$ were re-computed. The corrected wall spacing did not have a significant effect on the total forces and moments, although the FUN3D total forces and moments were slightly closer to the CFL3D results. The new FUN3D fine grid results fall within one to two symbol widths of the fine grid data plotted in Figs. 4(b) and (c).

One reason for the differences in CFL3D and FUN3D total forces and moment can be seen in Fig. 5 with a comparison of surface restricted streamlines on the Case 1 medium grids at $\alpha = 16°$. For Case 1 computations, flap separation occurs at all angles of attack, with FUN3D consistently predicting more separation than CFL3D. However, both codes show reduced flap separation with grid refinement. The differences in flap separation prediction may be due in part to the CFL3D solutions on the structured A grid series capturing wake profiles better than FUN3D solutions on the unstructured D grid series. Figure 6 shows a comparison of computed velocity profiles over the flap on the fine and medium grids at $\alpha = 7°$. The low Reynolds number $Re_c = 1.35 \times 10^6$ experimental data are also shown for reference. A comparison of grid density over the flap indicates that the structured grid has more resolution in the wake than the unstructured grid. Earlier comparisons of CFL3D and FUN3D results on the HiLiftPW-1 trapezoidal wing[29] showed a similar trend in the prediction of wake profiles and flap separation as for the current clean configuration.

Figures 7 and 8 show a comparison of computed (FUN3D) and experimental chordwise pressure distributions at two stations, mid-span ($\eta = 0.45$) and outboard ($\eta = 0.75$), over a range of angles of attack, $\alpha = 7°$ to $21°$. At the mid-span location, located away from slat and flap bracket influence, the experimental suction pressures on the slat and main elements increase with increasing angle of attack while the suction pressures on the flap decrease with increasing angle of attack. The experimental suction pressures on the aft end of the main element tend to decrease slightly with increasing angle of attack. The FUN3D computed results on the medium grid show a similar variation. The computed pressures on the slat and main match the experiment values well except at $\alpha = 21°$, where FUN3D over-predicts the suction values. The computed suction pressures on the flap are generally over-predicted at all angles of attack. At the outboard location (Fig. 8), which is located near the sixth slat and fourth flap brackets, the trend in experimental suction pressures with increasing angle of-attack is clearly different than the trend at the mid-span location. While the slat suction pressures in the experiment increase with angle of attack, the main element suction pressures only increase up to $\alpha = 18.5°$. The experimental suction pressures on the aft end of the main element also tend to decrease more significantly with increasing angle of attack. The experimental flap suction pressures consistently decrease with increasing angle of attack. In the computation, the slat and main element suction pressures continue to increase at higher angles of attack and the computed values are generally over-predicted, especially at the higher angles. The computed flap suction pressures indicate that the flow over the flap is separated on the aft end of the flap at $\alpha = 16°$ and above. The over-prediction of suction pressures on all the elements is consistent with the over-prediction of $C_{L,max}$ for Case 1.

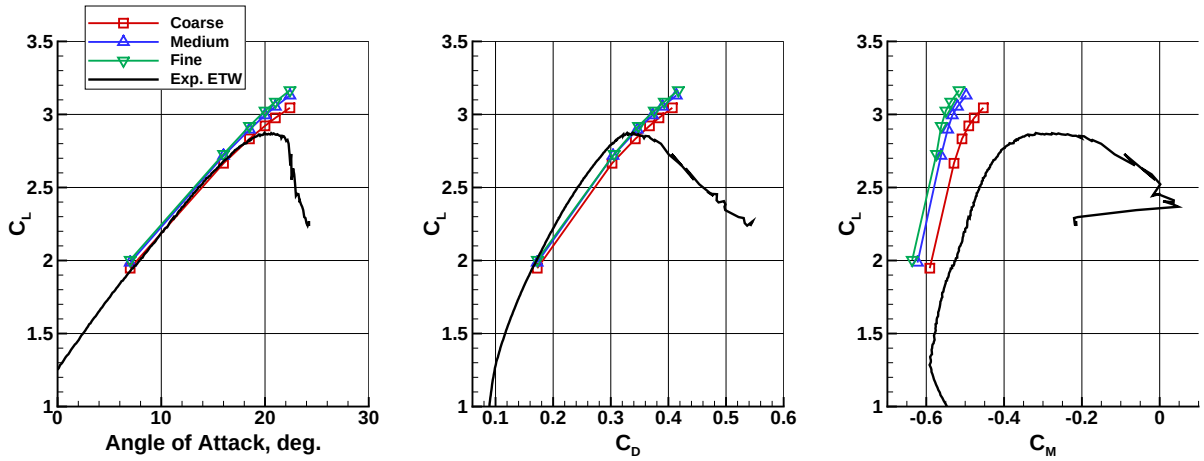

(a) CFL3D

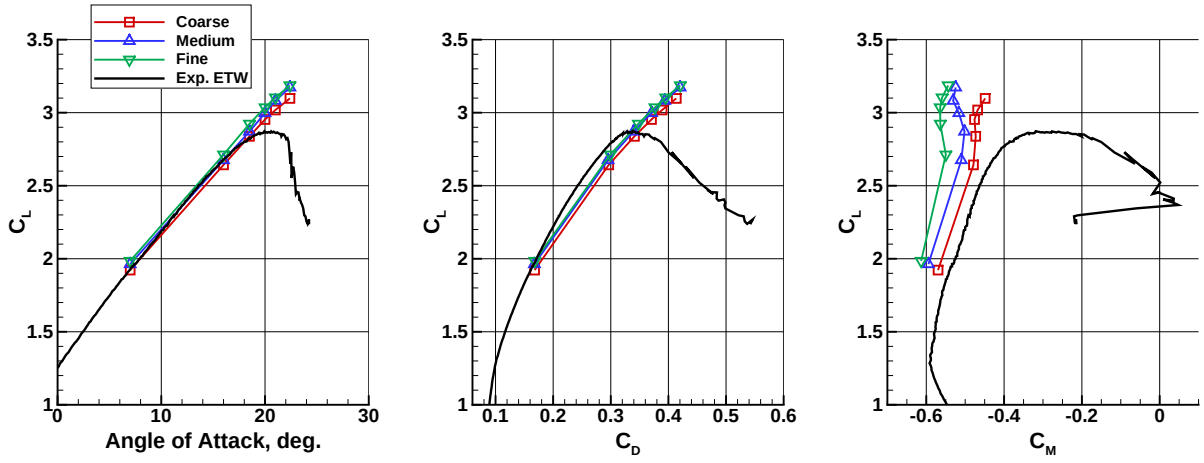

(b) FUN3D

Figure 3. Effect of grid density on Case 1 force and moment polars.

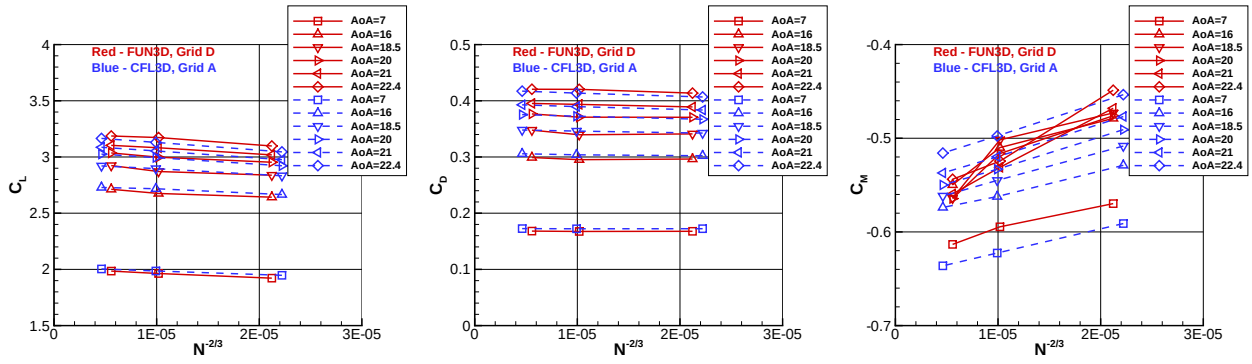

(a) all angles of attack

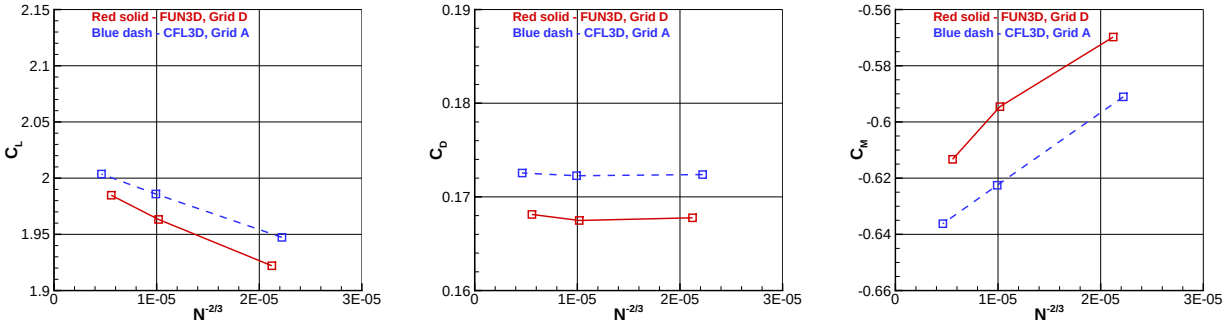

(b) $\alpha = 7^\circ$

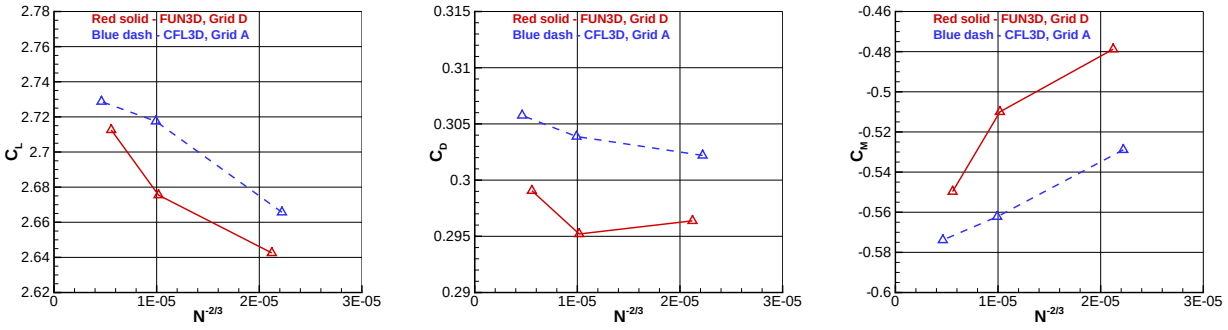

(c) $\alpha = 16^\circ$

Figure 4. Grid convergence of Case 1 total lift, drag and pitching moment coefficients.

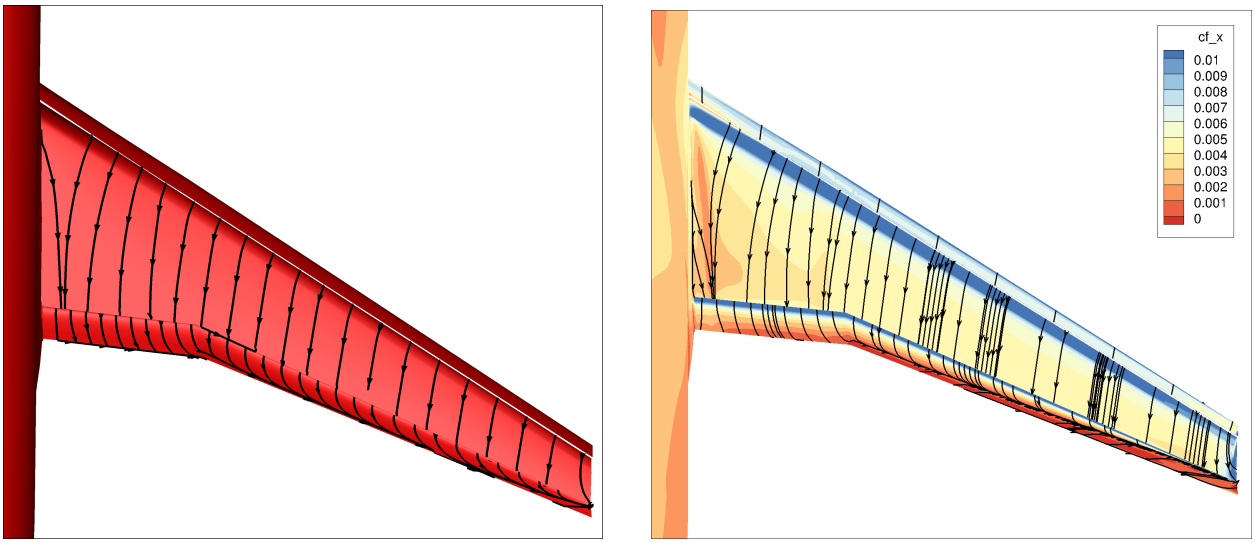

(a) CFL3D (b) FUN3D

Figure 5. Case 1 surface restricted streamlines on medium grids at $\alpha = 16^\circ$ (FUN3D includes contours of streamwise skin friction component).

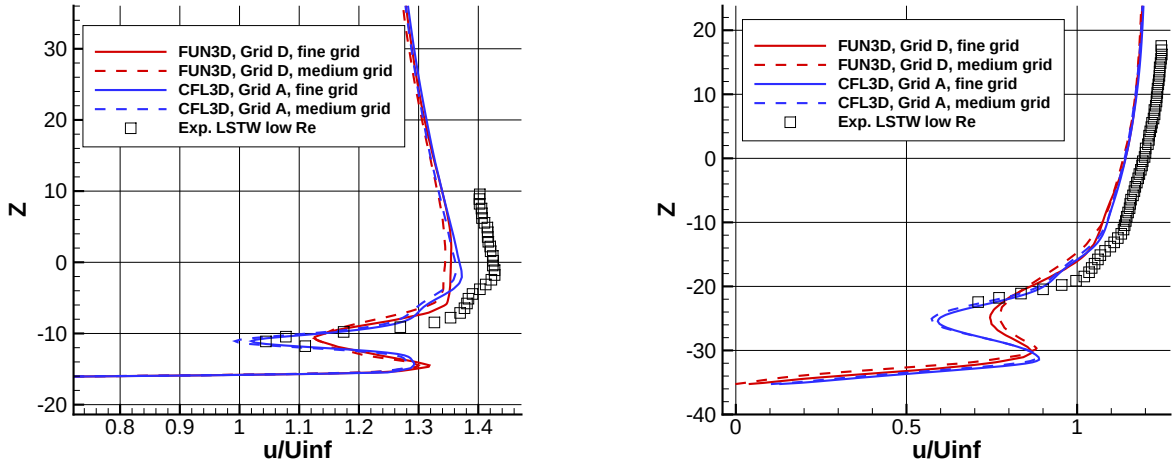

(a) plane 2, window E, line 1 (b) plane 2, window E, line 2

Figure 6. Case 1 velocity profiles over flap on fine and medium grids at $\alpha = 7^\circ$ ($Re_c = 1.35 \times 10^6$ exp. data shown for reference).

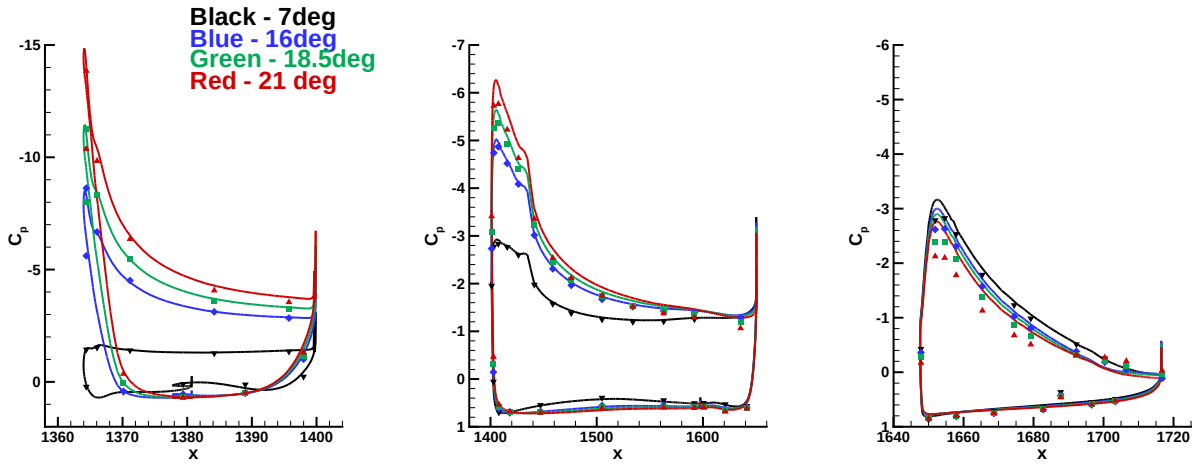

(a) slat (b) main (c) flap

Figure 7. Variation of Case 1 FUN3D chordwise pressure coefficient with angle of attack at span station $\eta = 0.45$ (symbols–exp., solid lines–computation.)

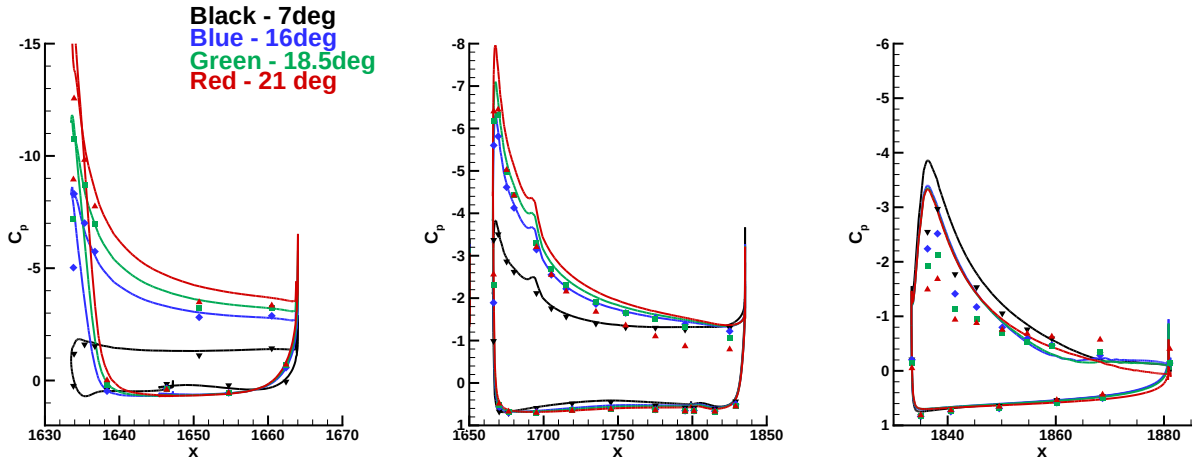

(a) slat (b) main (c) flap

Figure 8. Variation of Case 1 FUN3D chordwise pressure coefficient with angle of attack at span station $\eta = 0.75$ (symbols–exp., solid lines–computation.)

VI.A.2. Reynolds Number Effects Study (Case 2) with FUN3D

The effects of Reynolds number were explored using FUN3D for Config 4 (which includes support brackets) over a range of angles of attack: $\alpha = 0^\circ$ – 22.4°. Figure 9 shows the lift, drag and pitching moment polars on the workshop grid at both high and low Reynolds numbers. The FUN3D results with the SA turbulence model capture the general effect of the Reynolds number variation, but the $C_{L,max}$ is still not well predicted in comparison with the experimental data. Although stall is captured in the computations with the brackets included, the loss of lift at the higher angles of attack ($\alpha = 18^\circ$ – 20°) is more abrupt than in the experiment. The lift coefficient also is slightly under-predicted at $\alpha = 7^\circ$ – 16° with the brackets included. The drag coefficient continues to be over-predicted in comparison with the experiment. The lower Reynolds number computations are in closer agreement with experiment at the higher angles of attack. The nose-down pitching moment also continues to be over-predicted in comparison with the experiment at both Reynolds numbers. The pitching moment does, however, compare more favorably at the post-stall angles of attack than the clean configuration. The predictions of lift, drag and pitching moment for Case 2 are consistent with the majority of workshop submissions.[2]

As previously noted, oil visualization from the low Reynolds number experiment suggests that at stall large isolated areas of separated flow exist over the main wing behind two of the slat brackets (SB5 and SB6) and in front of two of the flap tracks (FB3 and FB4), which spread out laterally towards the trailing edge. Although oil flow visualization was not performed during the high Reynolds number test, the pressure measurements and force/moment trends indicate a similar stall mechanism takes place at the high Reynolds condition. A comparison of the oil flow measurement and the computed surface restricted streamlines help to illustrate the difference between the experimental and computed stall mechanisms. Figure 10 shows a comparison of the low-Reynolds number experimental oil flow and Case 2a surface restricted streamlines near maximum lift ($\alpha = 18.5^\circ$). The computation over-predicts the separation behind SB6 but fails to predict any separation behind SB5 at $\alpha = 18.5^\circ$.

A similar stall mechanism occurs in the computations for the higher Reynolds number Case 2b. Figures 11 and 12 show comparisons of Case 1 (medium grid) and Case 2b (medium grid) surface restricted streamlines before and after stall ($\alpha = 16^\circ$ and $\alpha = 20^\circ$). Without the brackets, the flow over the main wing stays attached at both angles of attack. When the brackets are included, the flow over the outboard flap at $\alpha = 16^\circ$ is less separated than on the clean wing. Also with brackets, the computation at $\alpha = 20^\circ$ predicts separation behind SB6 but fails to predict any separation behind SB5. A comparison of computed and experimental chordwise pressure distributions at $\eta = 0.45$ and $\eta = 0.75$ in Figs. 13 and 14 show that the separation behind SB6 is over-predicted at the higher angle of attack, $\alpha = 21^\circ$. Overall, the comparison of the pressures with the experiment at the inboard station is improved with the inclusion of the brackets. The flap suction pressures are still over-predicted. The comparison of pressures at the outboard station, $\eta = 0.75$, is also improved at the lower angles of attack, especially the variation in flap suction pressure with angle of attack. But the main wing separation is clearly over-predicted.

The effect of Reynolds number on the velocity profiles at $\alpha = 7^\circ$ is shown in Fig. 15. This figure shows a comparison of computed velocity profiles at the low and high Reynolds number conditions, Case 2a and 2b, with the low Reynolds number $Re_c = 1.35 \times 10^6$ experimental data also shown for comparison with Case 2a computations. The effect of Reynolds number on the velocity profiles appears to have the correct trend, but overall the low Reynolds number velocity profiles compare with the experiment only qualitatively. The slat and main element wakes do not appear to be sufficiently resolved on this grid at either Reynolds number.

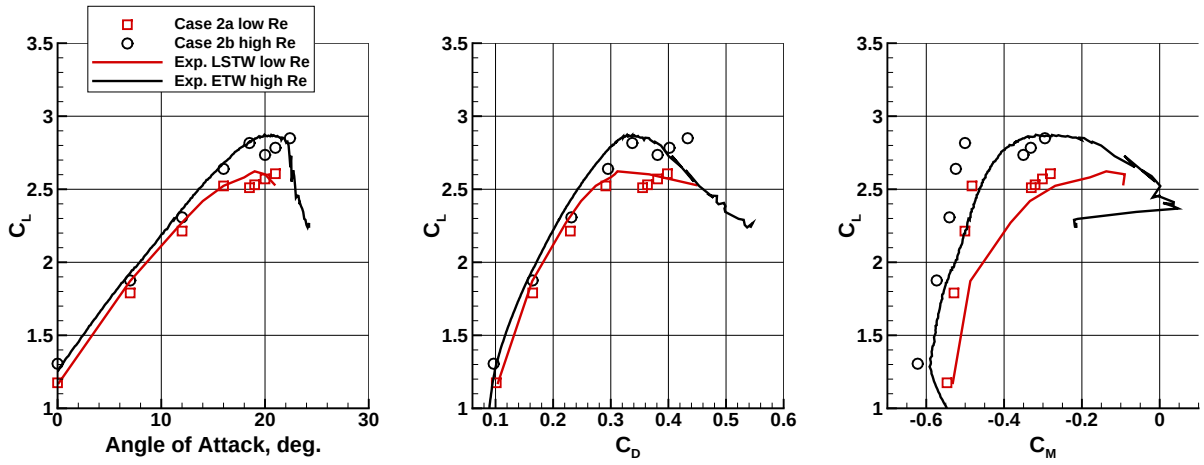

Figure 9. Effect of Reynolds number on Case 2 FUN3D force and moment polars.

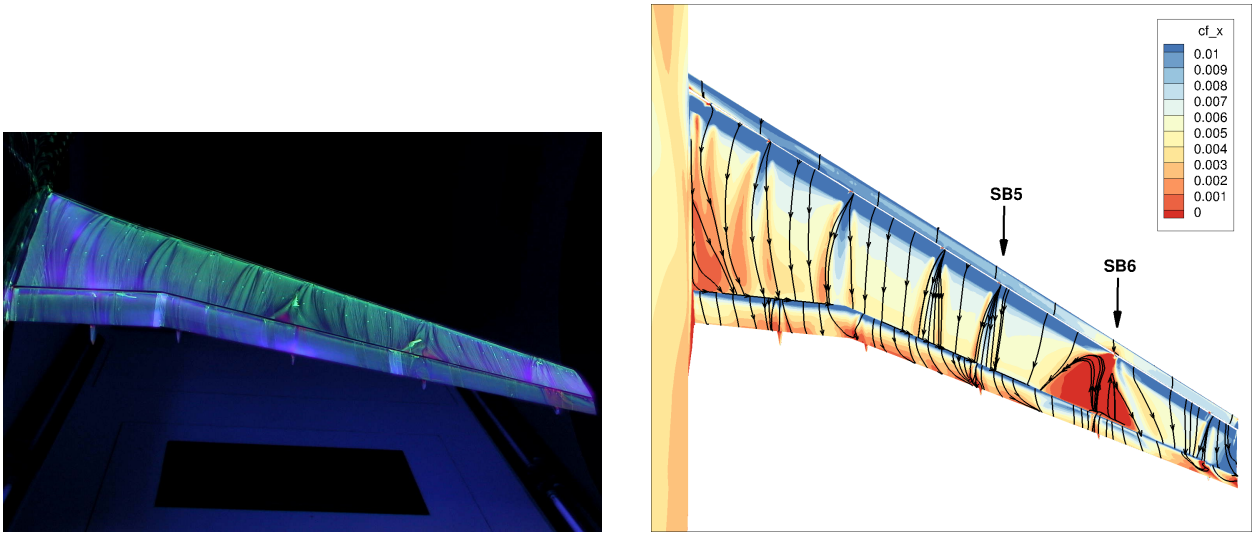

(a) Experiment

(b) Case 2a using FUN3D

Figure 10. Comparison of experimental oil flow and Case 2a FUN3D surface restricted streamlines at $\alpha = 18.5^{\circ}$ (computation includes contours of streamwise skin friction component).

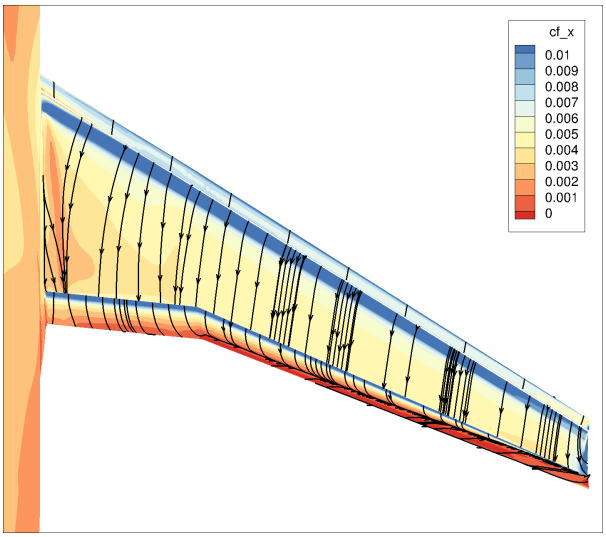

(a) Case 1

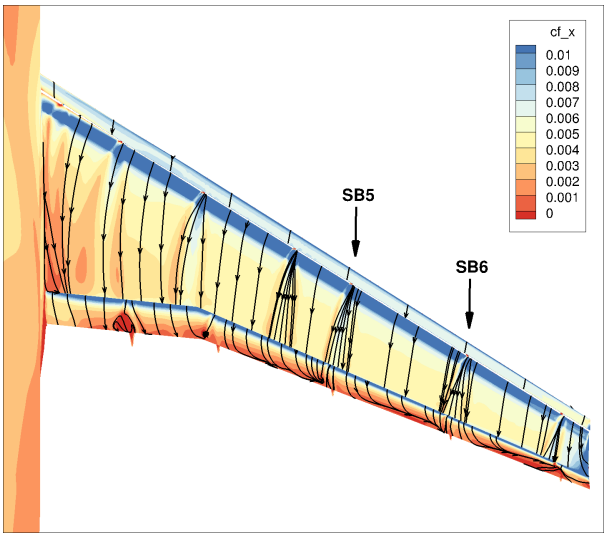

(b) Case 2b

Figure 11. Comparison of Case 1 (medium grid) and Case 2b FUN3D surface restricted streamlines $\alpha = 16^{\circ}$, with contours of streamwise skin friction component.

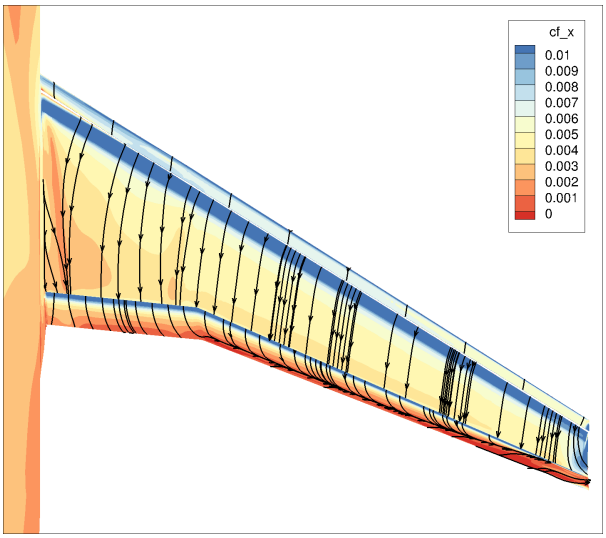

(a) Case 1

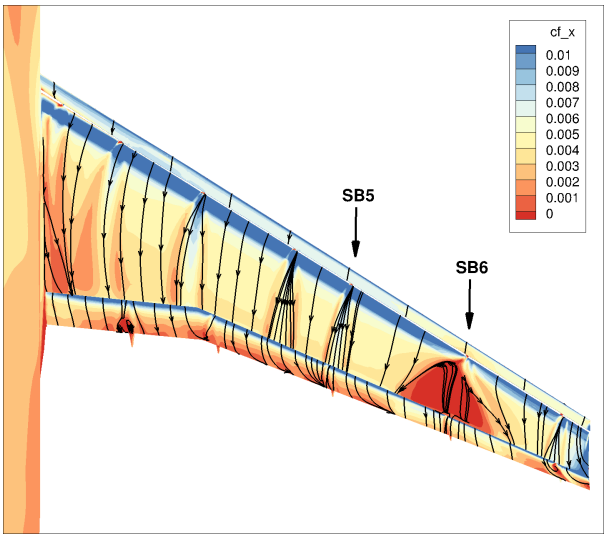

(b) Case 2b

Figure 12. Comparison of Case 1 (medium grid) and Case 2b FUN3D surface restricted streamlines at $\alpha = 20^{\circ}$, with contours of streamwise skin friction component.

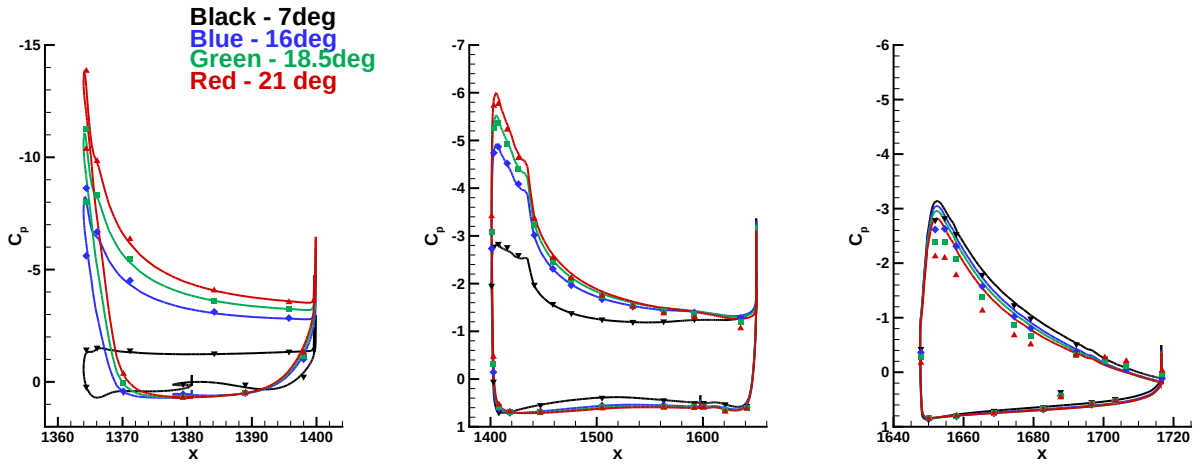

(a) slat (b) main (c) flap

Figure 13. Variation of Case 2b FUN3D chordwise pressure coefficient with angle of attack at span station $\eta = 0.45$ (symbols–exp., solid lines–computation.)

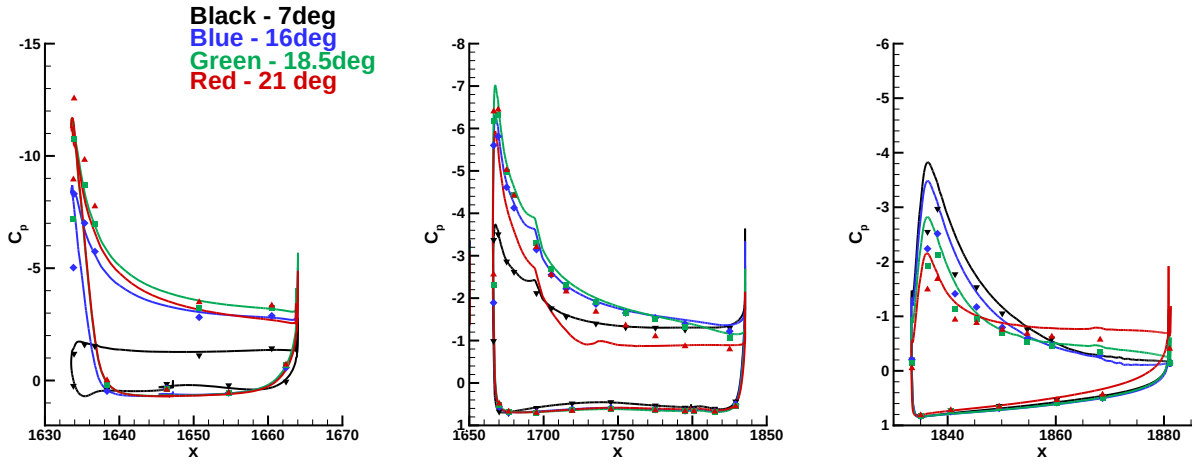

(a) slat (b) main (c) flap

Figure 14. Variation of Case 2b FUN3D chordwise pressure coefficient with angle of attack at span station $\eta = 0.75$ (symbols–exp., solid lines–computation).

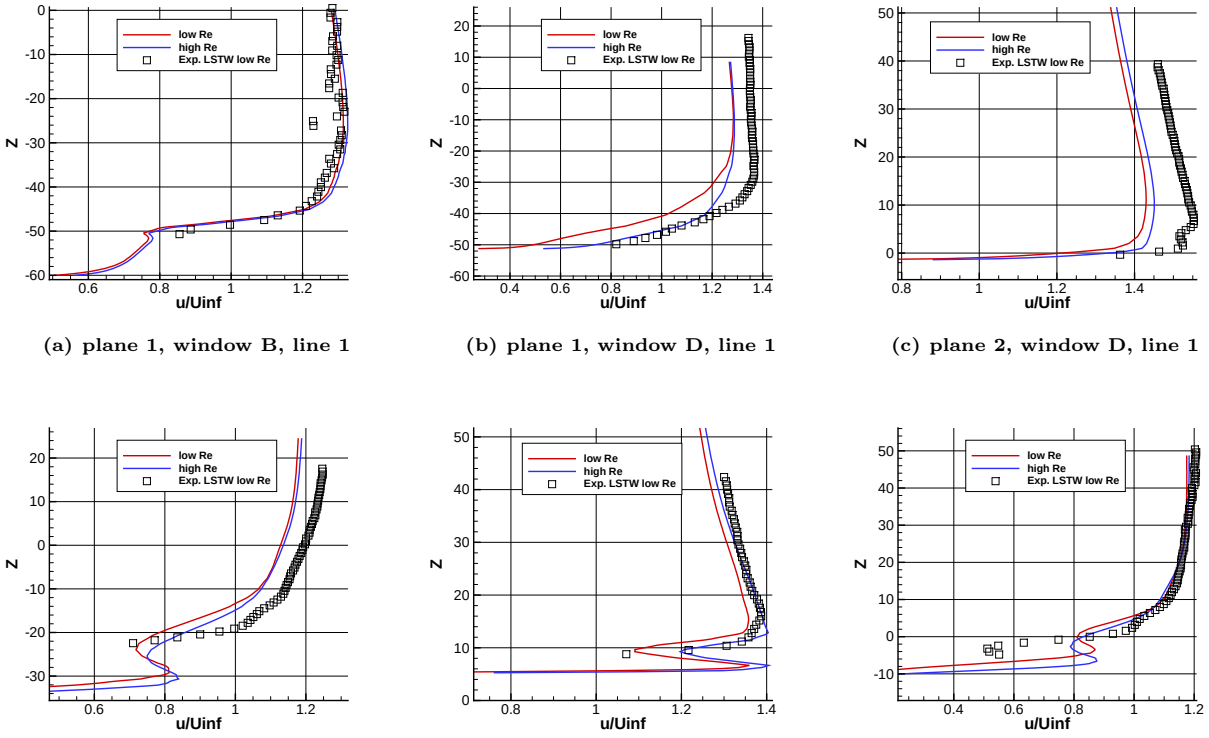

(a) plane 1, window B, line 1 **(b) plane 1, window D, line 1** **(c) plane 2, window D, line 1**

(d) plane 2, window E, line 2 **(e) plane 3, window E, line 1** **(f) plane 3, window E, line 2**

Figure 15. Case 2 FUN3D velocity profiles at $\alpha = 7^\circ$ for $Re_c = 1.35 \times 10^6$ and $Re_c = 15 \times 10^6$.

VI.A.3. Full Configuration Study (Case 3b) with FUN3D

The effects of pressure tube bundles were explored for Config 5 at $Re_c = 15 \times 10^6$ over a range of angles of attack: $\alpha = 7° - 22.4°$. The effect of the SAR model was also investigated for Config 5 because the current authors found in Ref. 35 that including the rotation variant of the SA model improved the prediction of tip pressures for the HiLiftPW-1 trapezoidal wing configuration. Figure 16 shows the Config 5 lift, drag and pitching moment polars for FUN3D on the workshop grid with both the SA and SAR turbulence model. The Case 2b results with the SA model are also shown in Fig. 16 for comparison. At the low angles of attack, the inclusion of the bundles does not have a significant effect on the total forces and moments in comparison with the Case 2b results, and the SAR turbulence model also does not have a significant effect. At higher angles of attack, the inclusion of the bundles causes the main wing to stall at a lower angle of attack ($\alpha = 18.5°$ versus $\alpha = 20°$ for Case 2b) with both SA and SAR models. A comparison of surface restricted streamlines (not shown here) indicates that the computed stall mechanism for Case 3b is similar to Case 2b in that there is an over-prediction of separation behind SB6 but no separation predicted behind SB5. However, the stall for Case 3b occurs at a lower angle of attack. The inclusion of the pressure tube bundles results in a less accurate prediction of lift near stall.

At an angle of attack below stall, only small variations in the surface pressures result from the use of the SA rotation variant, SAR. In contrast to the results of the HiLiftPW-1 shown in Ref. 35, the inclusion of the SA rotation variant (SAR) did not have as significant an impact on the prediction of the flow near the tip of the configuration. More noticeable variations are seen at the mid-span $\eta = 0.75$ location just inboard of the SB6 spanwise location due to the inclusion of the bundles. Figure 17 illustrates that at $\alpha = 16°$, inclusion of the bundles improves the comparison of the main and flap pressures with the experiment at $\eta = 0.75$. The impact of the SAR model at this span station is negligible. In Fig. 17, the chordwise pressure results with SA and SAR overlay each other. Although the impact of the bundles is small in terms of surface pressure variation before stall, there is clearly a more significant effect on the stall mechanism and surface pressures as the angle of attack is increased.

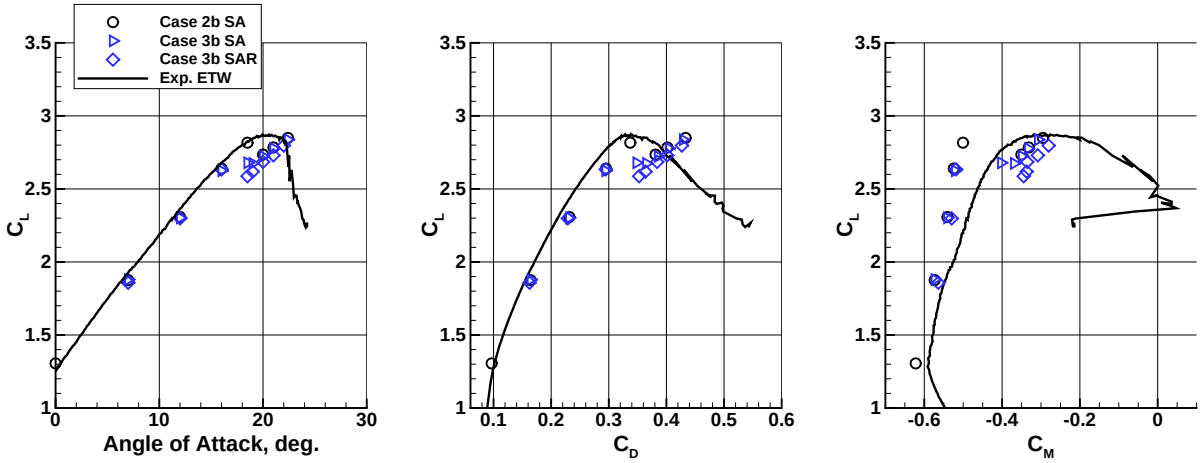

Figure 16. Effect of turbulence model on Case 3b FUN3D force and moment polars.

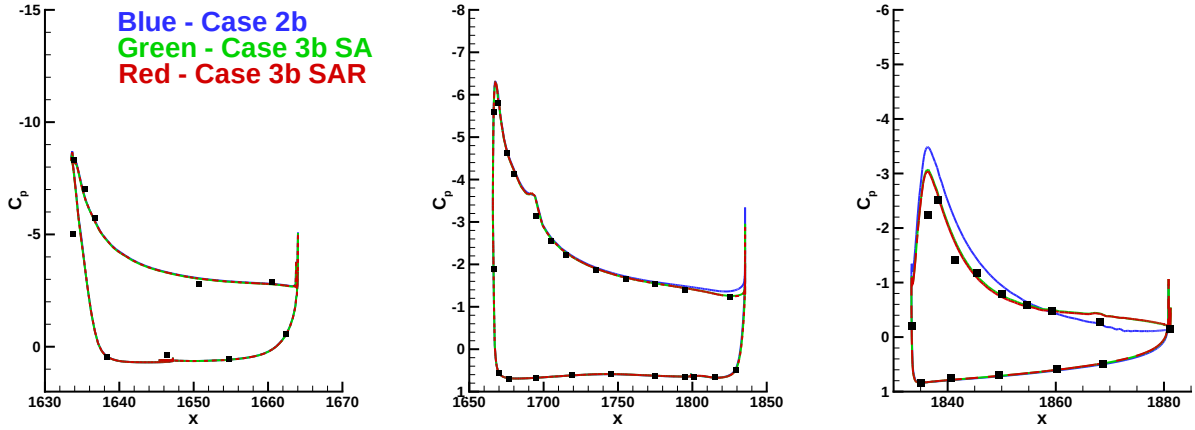

(a) slat (b) main (c) flap

Figure 17. Case 3b FUN3D $\eta = 0.75$ chordwise pressure coefficients at $\alpha = 16^\circ$ (symbols–exp., lines–computation.)

VI.B. Adaptive Grids with FUN3D

VI.B.1. Case 1 – Config 2

Although Config 2 computations are not expected to predict the stall mechanism, output-based adaptation was applied to the clean configuration at $\alpha = 16^\circ$ so that comparisons can be made between the adapted grid results and the results on the globally refined grids computed for Case 1. The Case 1 coarse and medium grids were used as a starting point for the off-body adaptation based on the output function L/D. The SA model was used for the adapted computations so that a direct comparison could be made with the workshop results. Four adaptation cycles were performed starting with the coarse and medium grids, requiring 8 additional adjoint and flow solutions. The final adapted coarse grid size was 16 million nodes, and the final adapted medium grid size was 62 million nodes. Figure 18 shows a comparison of C_L, C_D, and C_M as a function of grid size ($N^{-2/3}$) between the Case 1 workshop grids and the adapted grids. The variation of C_L, C_D, and C_M with off-body grid adaptation shows the same trends as global (surface and volume) refinement. However, local features had more significant changes.

A comparison of outboard flap chordwise pressure coefficients from medium and fine workshop grids and the adapted medium grid (Fig. 19) shows that the adapted grid predicts attached flow further outboard on the flap, which more closely matches the fine grid results and the experiment. The adapted medium grid pressures also match the fine grid suction pressure peaks on the flap. Figure 20 shows a comparison of Case 1 results from unadapted and adapted medium grids at $\eta = 0.70$ colored by contours of normalized streamwise velocity. The improved resolution of the slat and main element wakes can clearly be seen in the adapted grid contours. A more quantitative comparison of velocity profiles over the outboard main and flap elements is shown in Fig. 21. (Recall the wake profile locations shown in Fig. 2.) The slat and main wake profiles are significantly better resolved on the medium adapted grid. The adaptation also changes the boundary layer profile near the flap trailing edge at $\eta = 0.874$ (3E2) resulting in less reversed flow than on the unadapted grid.

A computation at $\alpha = 16^\circ$ was performed on the final SA adapted medium grid to study the impact of the SAR model when flow features were resolved. When the rotation variant was included in the computation on the adapted grid, the prediction of the outboard flap pressures near $\eta = 0.89$ was significantly improved as shown in Fig. 22. While the effect of the SAR model on the workshop grid computations (shown earlier) was limited, the use of the SAR model improved the prediction of outboard pressures on the adapted grid. For this reason, the SAR model is used in subsequent Case 2b and 3b computations with adapted grids.

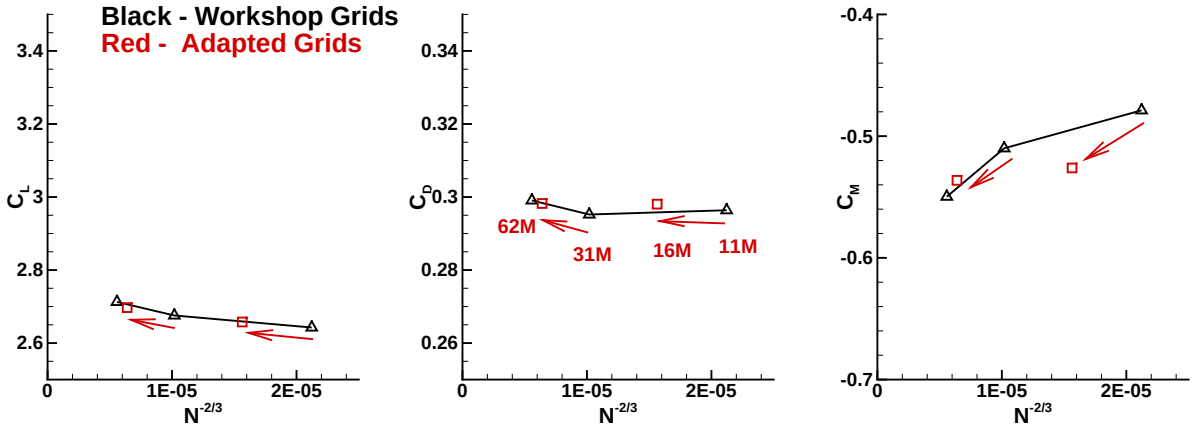

Figure 18. Comparison of total forces and moment at $\alpha = 16^\circ$ between Case 1 FUN3D workshop grids and adapted grids.

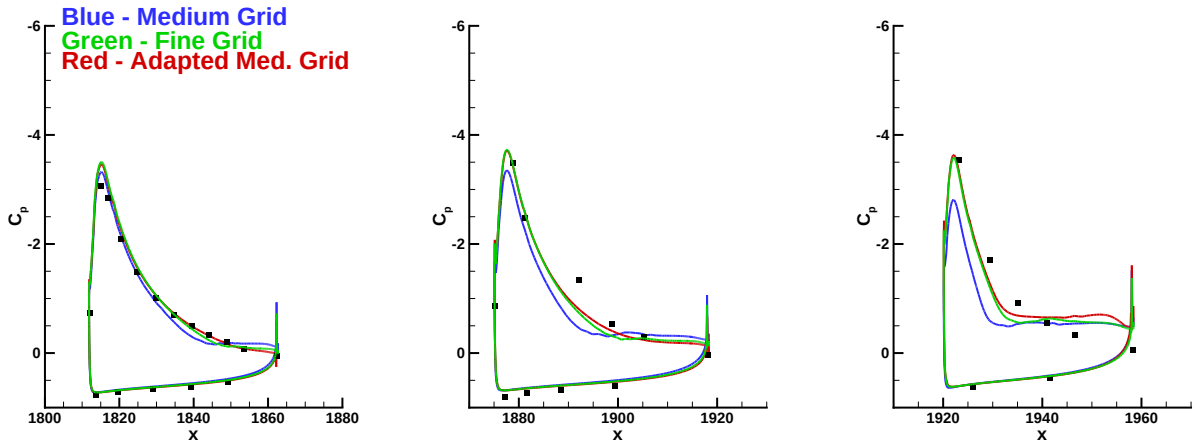

(a) $\eta = 0.72$ **(b)** $\eta = 0.82$ **(c)** $\eta = 0.89$

Figure 19. Comparison of Case 1 FUN3D outboard flap chordwise pressure coefficients from unadapted and adapted grids at $\alpha = 16°$.

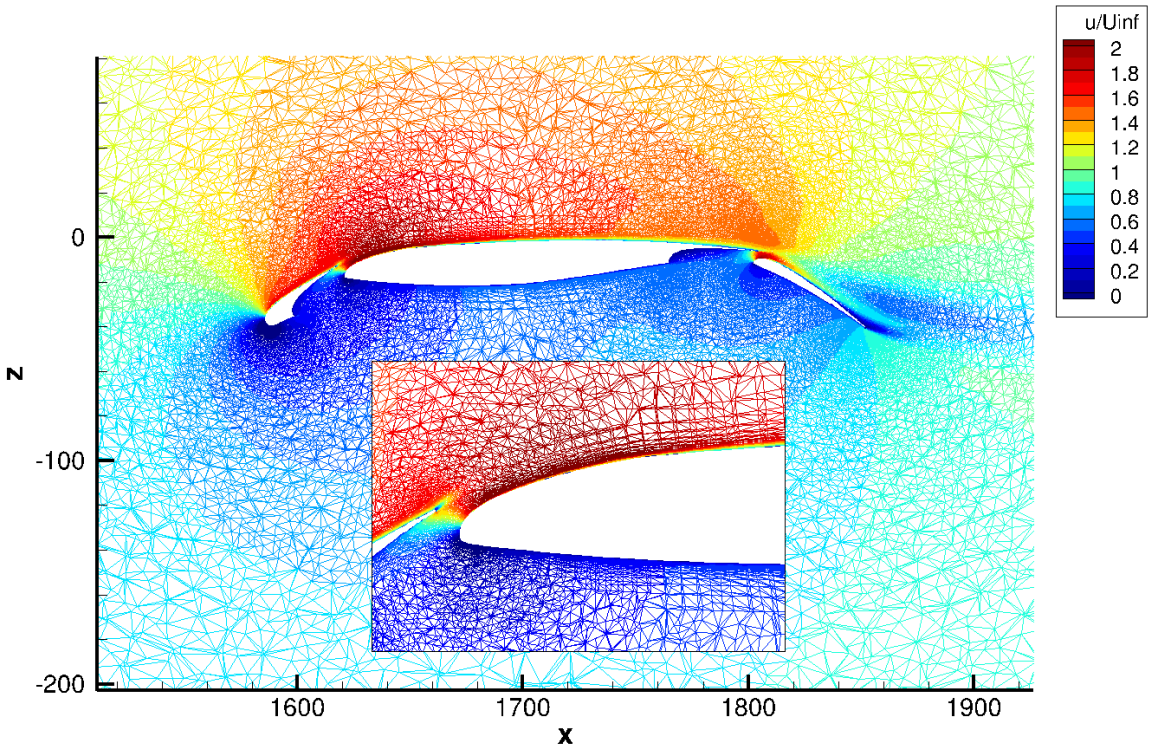

(a) unadapted grid - 31 million nodes

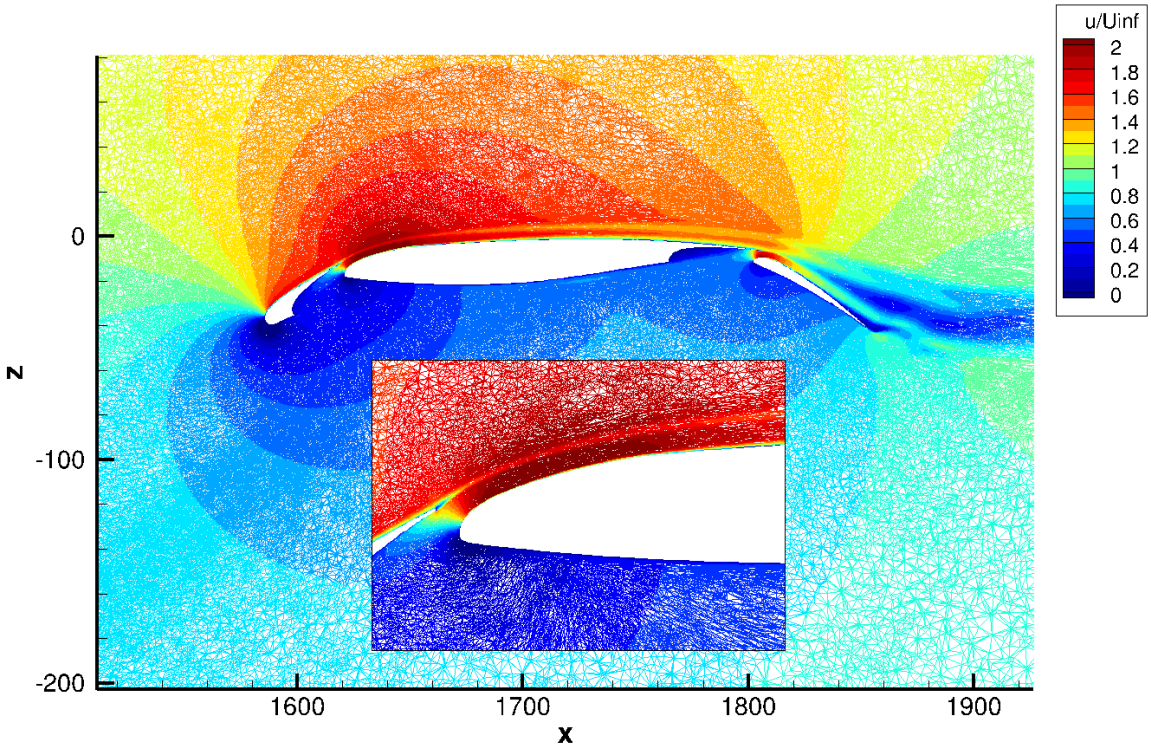

(b) adapted grid - 62 million nodes

Figure 20. Comparison of unadapted and adapted medium grids from Case 1 FUN3D at span station $\eta = 0.70$ and $\alpha = 16^\circ$ (grid colored by contours of normalized streamwise velocity).

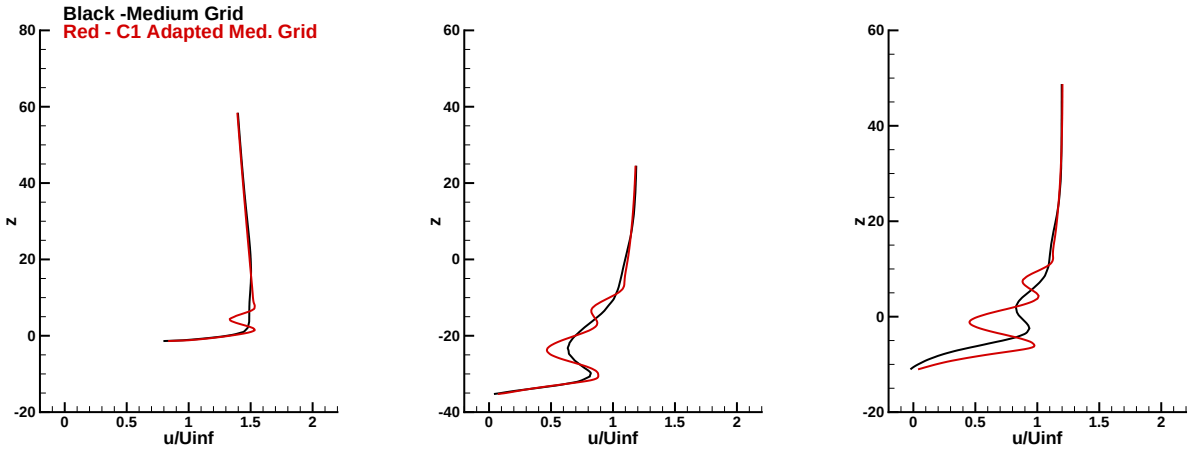

(a) plane 2, window D, line 1 (b) plane 2, window E, line 2 (c) plane 3, window E, line 2

Figure 21. Comparison of Case 1 FUN3D velocity profiles from unadapted and adapted medium grids at $\alpha = 16^\circ$

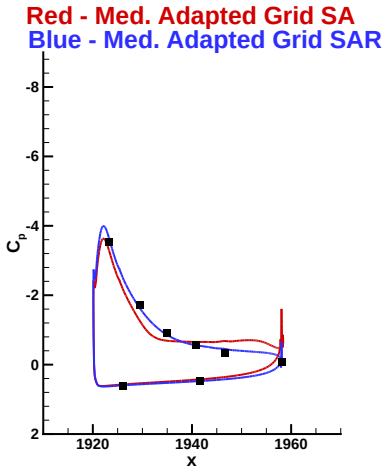

(a) $\eta = 0.89$

Figure 22. Effect of turbulence model on Case 1 FUN3D outboard flap chordwise pressure coefficients from adapted medium grid at $\alpha = 16^\circ$ (symbols–exp., solid lines–computation).

VI.B.2. Case 2b – Config 4

Output-based adaptation was applied to Config 4 for the high Reynolds number conditions (Case 2b) at several angles of attack approaching $C_{L,max}$. The Case 2b medium grid was used as a starting point for the off-body adaptation based on the output function L/D. For the reasons noted in the previous section, the SAR model was used for the adapted computations. At $\alpha = 16°$, four adaptation cycles were performed starting with the medium workshop grid, requiring four additional adjoint and flow solutions. The final adapted grid size at $\alpha = 16°$ was 58 million nodes. The $\alpha = 18.5°$ solution was restarted from the final adapted-grid solution at $\alpha = 16°$, and two adaptation cycles were performed. The final adapted grid size at $\alpha = 18.5°$ was 78 million nodes. Solutions at $\alpha = 19°$, 20° and 21° were computed on the adapted grid from final $\alpha = 18.5°$ adaptation cycle. Each solution was initialized from the previously converged computation at a lower angle of attack.

Figure 23 shows a comparison of computed C_L, C_D, and C_M polars between the Case 2b workshop grid (SA) and the adapted grids (SAR). At $\alpha = 16°$ and 18.5°, the grid adaptation does not significantly affect the global forces and moments. However with grid adaptation, the lift is no longer under-predicted at the higher angles of attack. The computed lift continues to increase with increase in angle of attack and is over-predicted in comparison with the experiment. Figure 24 shows the surface restricted streamlines for the Case 2b adapted grid solutions at $\alpha = 18.5°$ and 20°. These solutions show no significant separation (reverse flow) behind either SB5 or SB6. (Recall from Fig. 12, the Case 2b computation at $\alpha = 20°$ on the workshop grid showed significant separation behind SB6.)

Figures 25 and 26 show a comparison of computed and experimental chordwise pressure distributions at two stations, mid-span $\eta = 0.55$ and outboard $\eta = 0.75$, over the range of computed angles of attack for the adapted grids. The mid-span location is nearest to the SB5 span location while the outboard location is nearest to the SB6 span location. At these angles of attack, the Case 2b prediction of pressure with the adapted grids is closer to the experiment, especially on the main element at $\eta = 0.75$. However, the suction pressure is over-predicted on the aft part of the main element at $\alpha = 21°$, possibly indicating that the experiment has separated flow on the main element behind SB6 while the computation shows no separation. The main element pressure predictions match the experiment very well at $\eta = 0.55$ near SB5 possibly indicating that in the experiment the high-Reynolds number flow does not separate behind SB5 as much as at the lower Reynolds number. The flap leading-edge suction peaks continue to be over-predicted. However in comparison with the solutions on the workshop grid (Fig. 14), the prediction of flap pressures on the adapted grids is much closer to the experiment, although some of the improvement may be attributed to the SAR model.

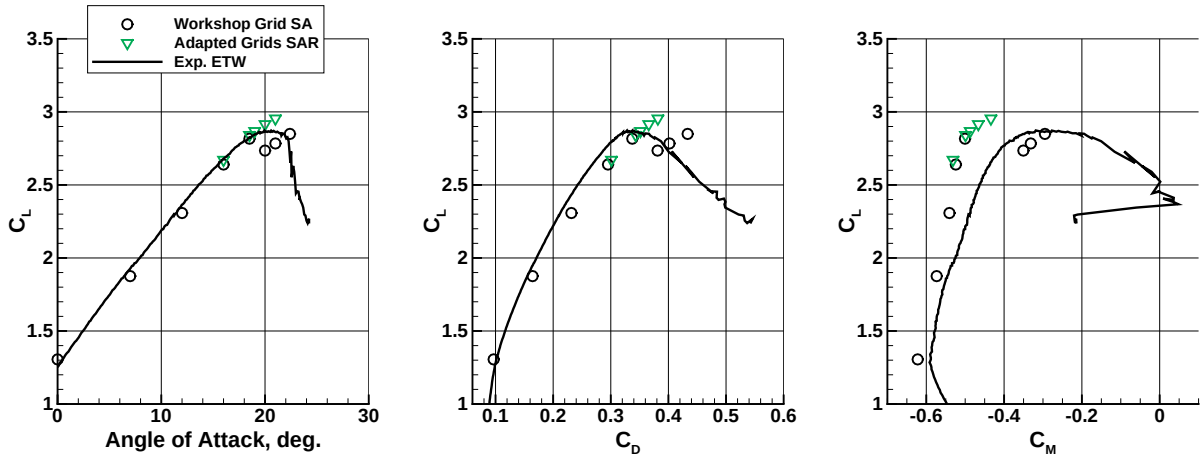

Figure 23. Comparison of total forces and moment polars between Case 2b workshop grid and adapted grids.

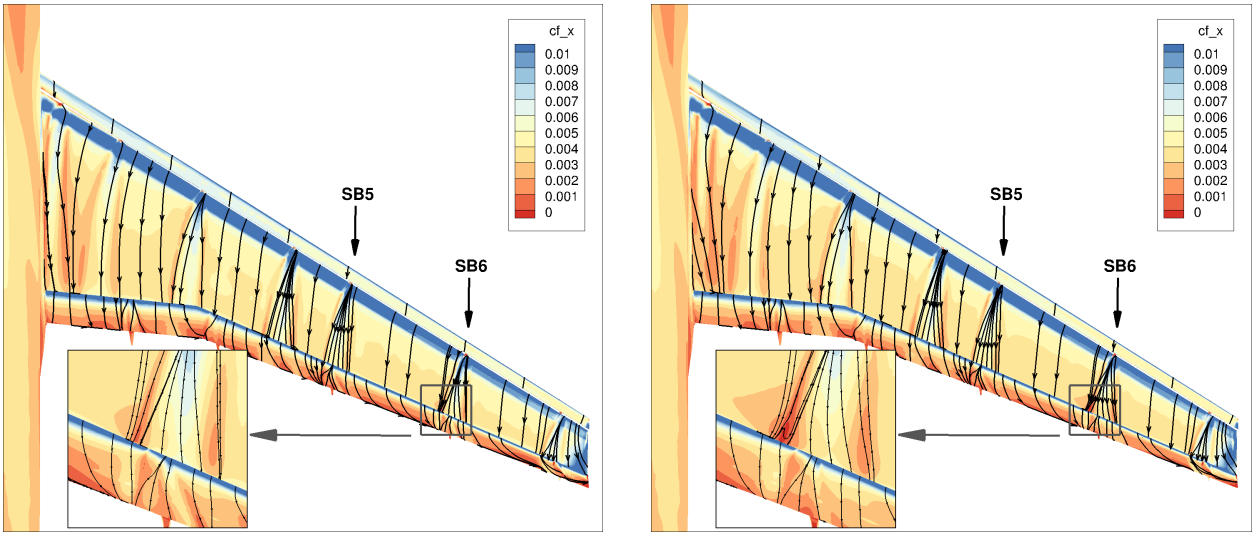

(a) $\alpha = 18.5°$ **(b)** $\alpha = 20°$

Figure 24. Comparison of Case 2b adapted grid surface restricted streamlines near stall, with contours of streamwise skin friction component.

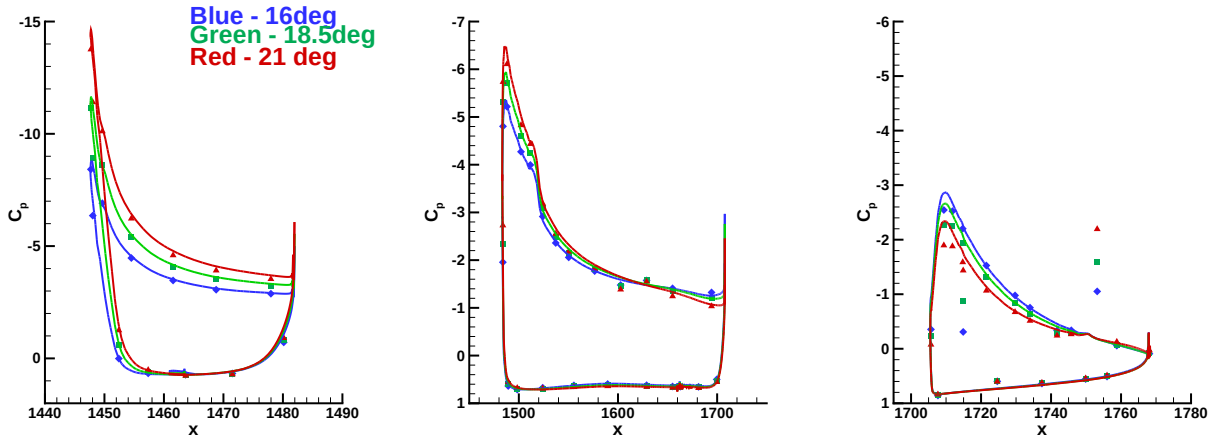

(a) slat **(b) main** **(c) flap**

Figure 25. Variation of Case 2b $\eta = 0.55$ chordwise pressure coefficients with angle of attack on adapted grids (symbols–exp., solid lines–computation).

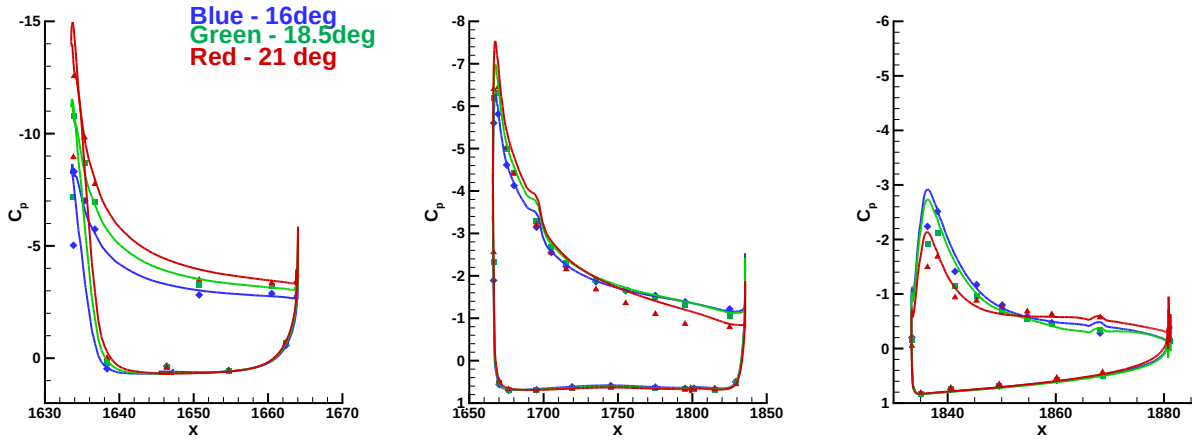

(a) slat (b) main (c) flap

Figure 26. Variation of Case 2b $\eta = 0.75$ chordwise pressure coefficients with angle of attack on adapted grids (symbols–exp., solid lines–computation).

VI.B.3. Case 3b – Config 5

A similar process was used in the computation of output-based adapted solutions for Config 5. Adjoint-based adaptation was applied to Config 5 at several angles of attack approaching $C_{L,max}$. The Case 3b medium grid was used as a starting point for the off-body adaptation based on the output function L/D, and the SAR model was used for the adapted computations. Constant complexity scaling was applied to the scaling metric at $\alpha = 18.5°$ to improve the robustness of the adaption process. The final adapted grid size at $\alpha = 16°$ was 58 million nodes. The final adapted grid size at $\alpha = 18.5°$ was 93 million nodes. Solutions at $\alpha = 19°$ and 20° were computed on the adapted grid from the final $\alpha = 18.5°$ adaptation cycle. Each solution was initialized from the previously converged computation at a lower angle of attack. The flow solution at 21° failed to converge.

Figure 27 shows a comparison of computed C_L, C_D, and C_M between the Case 3b workshop grid (SAR) and the adapted grids (SAR). At $\alpha = 16°$, the grid adaptation does not significantly affect the global forces and moments. However with grid adaptation, the lift is no longer under-predicted at the higher angles of attack. The computed lift continues to increase with increase in angle of attack and is in close comparison with the experiment. Figure 28 shows the surface restricted streamlines for the Case 3b adapted grid solutions at $\alpha = 18.5°$ and 20°. These solutions show no separation (reverse flow) behind SB5, but small pockets of separated flow are predicted behind SB6 near the trailing edge. This pocket of separated flow grows slightly from $\alpha = 18.5°$ to $\alpha = 20°$. When grid adaptation is used, the inclusion of the pressure tube bundles results in a more accurate prediction of lift near stall. This is in contrast to the effect seen when comparing results on the workshop grids.

Figures 29 and 30 show a comparison of computed and experimental chordwise pressure distributions at $\eta = 0.55$ and $\eta = 0.75$ over the range of computed angles of attack for the adapted grids. At these angles of attack, the overall prediction of pressure with the adapted grids is very close to the experiment. The suction pressure is now well predicted on the aft part of the main element at $\alpha = 20°$. The flap leading-edge suction peaks continue to be over-predicted. However in comparison with the solutions on the workshop grid (Fig. 17), the prediction of flap pressures on the adapted grids is much closer to the experiment. A follow-on study should be done to determine the influence of surface refinement on the Case 3b adapted results.

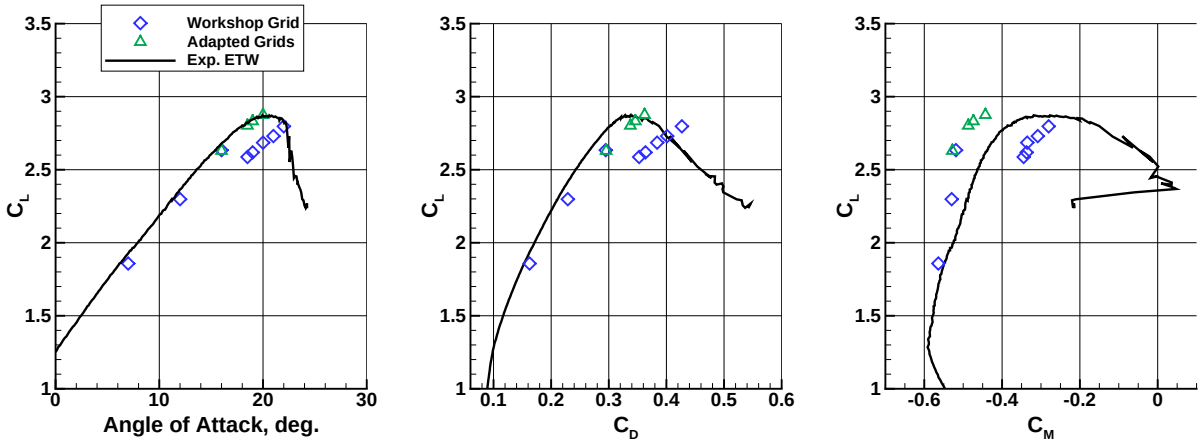

Figure 27. Comparison of total forces and moment polars between Case 3b workshop grid and adapted grids with SAR.

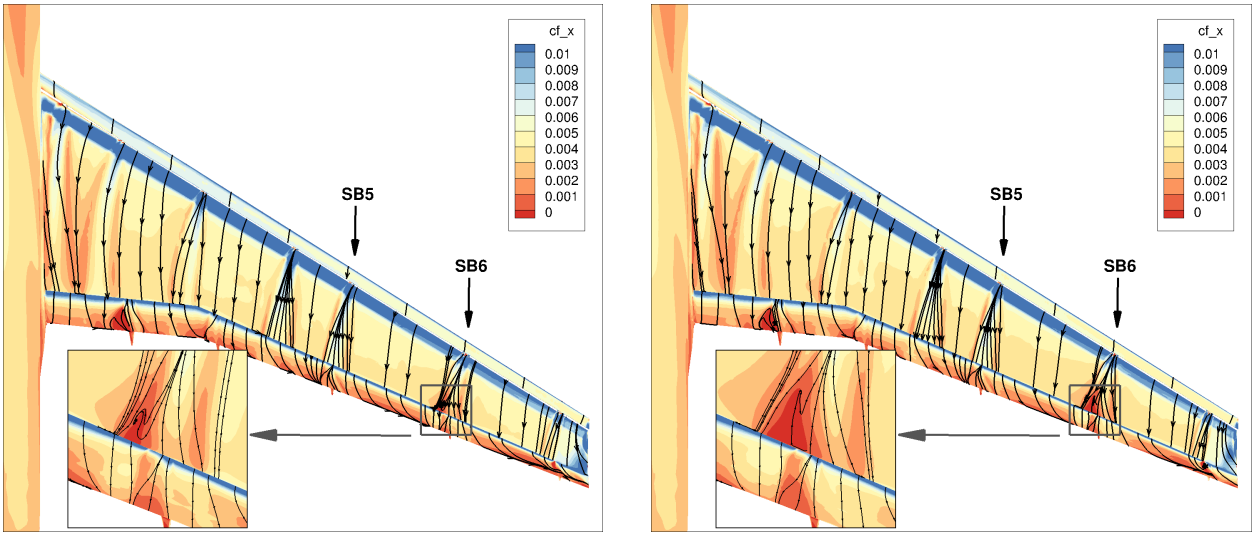

(a) $\alpha = 18.5°$ **(b)** $\alpha = 20°$

Figure 28. Comparison of Case 3b adapted grid surface restricted streamlines near stall, with contours of streamwise skin friction component.

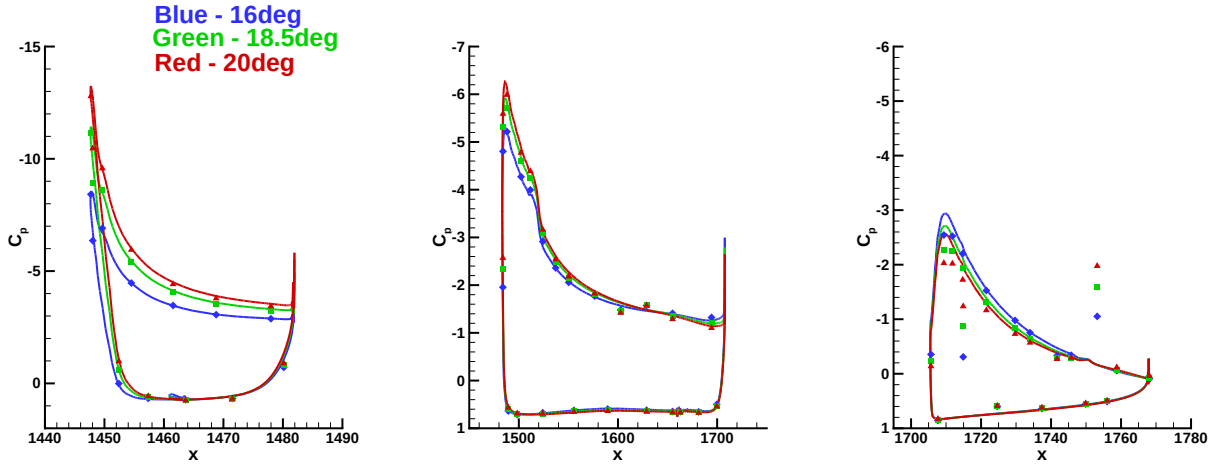

(a) slat **(b) main** **(c) flap**

Figure 29. Variation of Case 3b $\eta = 0.55$ chordwise pressure coefficients with angle of attack on adapted grids (symbols–exp., solid lines–computation).

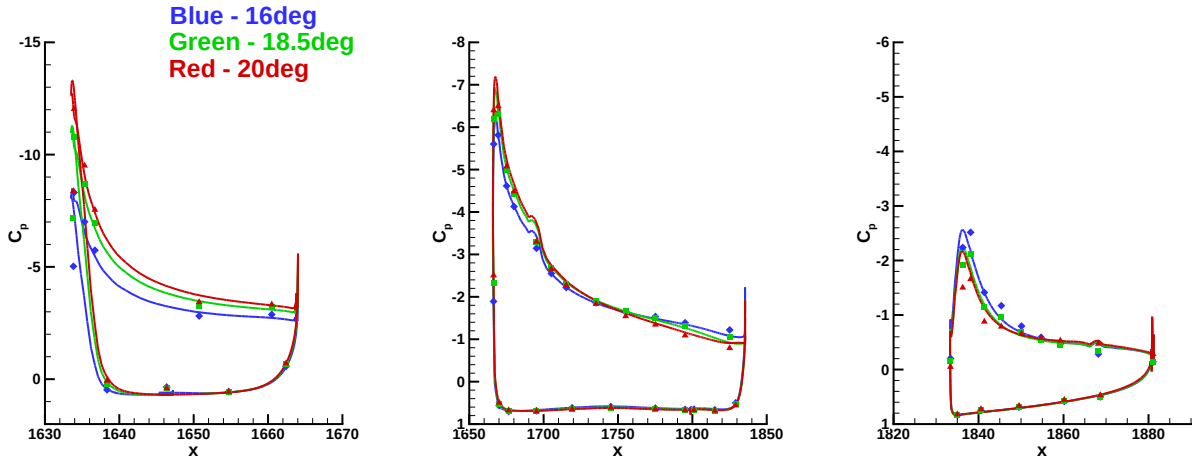

(a) slat (b) main (c) flap

Figure 30. Variation of Case 3b $\eta = 0.75$ chordwise pressure coefficients with angle of attack on adapted grids (symbols–exp., solid lines–computation).

VII. Conclusions

Contributions of the unstructured Reynolds-averaged Navier-Stokes code FUN3D to the 2nd AIAA CFD High Lift Prediction Workshop were described, and detailed comparisons were made with experimental data as well as with results from a second code (CFL3D) on the clean wing configuration. A grid convergence study and a Reynolds number study were conducted on workshop-supplied grids. Additional results for the high-Reynolds number, full configuration study were computed with FUN3D on workshop-supplied grids. Output-based, off-body grid adaptation was applied to the FUN3D solutions for a selected number of configurations and angles of attack, exploring the influence of automated grid refinement, geometry, and a turbulence model rotation correction. The computations with output-adapted grids follow the current state-of-the-art for CFD applied to high-lift applications, and represent active development at the leading edge of CFD capabilities. The following observations can be made based on the results of the current computational study:

(1) Grid Convergence Study (clean wing): On the workshop-supplied series A and D grids, the structured grid and unstructured grid results with the same turbulence model (SA) compared reasonably well in total forces/moments. There was flap separation at all angles of attack, and the FUN3D solutions on the unstructured D grids showed more flap separation than CFL3D solutions on the structured A grids. On the clean wing, the $C_{L,max}$ was over-predicted for both codes, and at higher angles of attack, there were larger differences between codes (especially in the moment coefficient). CFL3D solutions on the structured A grid series captured the wake profiles better than FUN3D on the unstructured D grid series. The total forces and moment variation with grid adaptation on the clean wing showed similar trends to global grid refinement. The slat and main wake profiles were significantly better resolved on the adapted grids, and the use of the SAR variant of the SA model improved the prediction of outboard pressures.

(2) Reynolds number study (with slat and flap brackets): On the workshop-supplied grid, the FUN3D results with the SA turbulence model captured the general effect of the Reynolds number variation, but the $C_{L,max}$ was under-predicted in comparison with the experimental data due to excessive main element separation behind one of the outboard slat brackets. However, below stall the comparison of computed results (forces, moments, surface pressures) with the experiment was improved with the inclusion of the brackets. On the workshop-supplied grid, the effect of Reynolds number on the velocity profiles appears to have the correct trend, but overall the low Reynolds number velocity profiles compare with the experiment only qualitatively. The slat and main element wakes did not appear to be resolved on the D series grid at either Reynolds number. With grid adaptation and SAR, the lift was no longer under-predicted at the higher angles of attack. The computed lift continued to increase with angle of attack and was over-predicted in comparison with the experiment. The computations on the adapted grids had no significant main element separation behind the slat brackets at the higher angles of attack.

(3) Full configuration study (with brackets and slat pressure tube bundles): On the workshop-supplied grid, the inclusion of the pressure tube bundles resulted in a less accurate prediction of lift near stall, with excessive main element stall at a lower angle of attack than was seen without the bundles. However, below stall the comparison of computed results (forces, moments, surface pressures) with the experiment was improved with bundles and with the use of the SA rotation variant, SAR. When grid adaptation was used, the inclusion of the pressure tube bundles resulted in a more accurate prediction of lift near stall. This was in contrast to the effect seen when comparing results on the workshop grids. The computed lift continued to increase with increase in angle of attack and was in close agreement with the experiment. The computations on the adapted grids showed a small amount of main element separation behind the slat bracket at the higher angles of attack.

These results point to the need for (1) proper representation of all influential geometry components, (2) sufficient grid resolution, and (3) turbulence modeling that accounts for relevant physics, when attempting to predict $C_{L,max}$ on high-lift configurations. The use of grid adaptation will no doubt be an important component of most future large-scale computations. The ability to automatically add grid resolution in areas of the flow field where it is needed removes the need for human intervention and economizes computational resources.

VIII. Acknowledgments

The authors wish to thank Mujeeb R. Malik, Technical Lead of Revolutionary Computational Aerosciences in the NASA Fundamental Aeronautics Program, for his continued support. The authors also wish to thank Leonel Serrano, Raul Mendoza, Karuna Rajagopa, Neal Harrison, Yoram Yadlin, and John Vassberg of Boeing for their efforts in generating the Series A structured grids, and Mark Chaffin (Cessna Aircraft) and Michael Long (University of Wyoming) for their efforts in generating the Series D unstructured grids. All computations were performed on the NAS Pleiades supercomputer at NASA Ames Research Center.

References

[1]Rumsey, C. L., Slotnick, J. P., Long, M., Stuever, R. A., and Wayman, T. R., "Summary of the First AIAA CFD High Lift Prediction Workshop," *AIAA Journal of Aircraft*, Vol. 48, No. 6, Nov.-Dec. 2011, pp. 2068–2079.

[2]Rumsey, C. L. and Slotnick, J. P., "Overview and Summary of the Second AIAA High Lift Prediction Workshop (Invited)," AIAA Paper 2014-0747, Jan. 2014.

[3]Mavriplis, D., Long, M., Lake, T., and Langlois, M., "NSU3D Results for the Second AIAA High Lift Prediction Workshop," AIAA Paper 2014-0748, Jan. 2014.

[4]Chitale, K. C., Rasquin, M., Martin, J., and Jansen, K. E., "Finite Element Flow Simulations of the EUROLIFT DLR-F11 High Lift Configuration," AIAA Paper 2014-0749, Jan. 2014.

[5]Eliasson, P. and Peng, S.-H., "Results from the 2^{nd} AIAA CFD High Lift Prediction Workshop using Edge," AIAA Paper 2014-0750, Jan. 2014.

[6]Hanke, J., Shankara, P., and Snyder, D., "Numerical Simulation of DLR-F11 High Lift Configuration from HiLiftPW-2 using STAR-CCM+," AIAA Paper 2014-0914, Jan. 2014.

[7]Rudnik, R. and Melber-Wilkending, S., "DLR Contribution to the 2nd High Lift Prediction Workshop," AIAA Paper 2014-0915, Jan. 2014.

[8]Cavallo, P. A., "CRUNCH CFD Calculations for HiLiftPW-2 with Discretization Error Predictions," AIAA Paper 2014-0916, Jan. 2014.

[9]Deloze, T. and Laurendeau, E., "NSMB Contribution to the 2^{nd} High Lift Prediction Workshop," AIAA Paper 2014-0913, Jan. 2014.

[10]Allaneau, Y., Goldberg, U., Chakravarty, S., and Peroomian, O., "Contribution from Metacomp Technologies, Inc. to the Second High Lift Prediction Workshop," AIAA Paper 2014-0912, Jan. 2014.

[11]König, G., Fares, E., and Nölting, S., "Lattice-Boltzmann Flow Simulations for the HiLiftPW-2," AIAA Paper 2014-0911, Jan. 2014.

[12]Krist, S. L., Biedron, R. T., and Rumsey, C. L., "CFL3D User's Manual (Version 5.0)," NASA TM 208444, NASA Langley Research Center, June 1998.

[13]Roe, P. L., "Approximate Riemann Solvers, Parameter Vectors, and Difference Schemes," *Journal of Computational Physics*, Vol. 43, 1981, pp. 357–372.

[14]Spalart, P. R. and Allmaras, S. R., "A One-Equation Turbulence Model for Aerodynamic Flows," *Recherche Aerospatiale*, Vol. 1, No. 1, 1994, pp. 5–21.

[15]Menter, F. R., "Two-Equation Eddy-Viscosity Turbulence Models for Engineering Applications," *AIAA Journal*, Vol. 32, No. 8, Aug. 1994, pp. 1598–1605.

[16]Langtry, R. B. and Menter, F. R., "Correlation-Based Transition Modeling for Unstructured Parallelized Computational Fluid Dynamics Codes," *AIAA Journal*, Vol. 47, No. 12, Dec. 2009, pp. 2894–2906.

[17]Anderson, W. K. and Bonhaus, D. L., "An Implicit Upwind Algorithm for Computing Turbulent Flows on Unstructured Grids," *Computers and Fluids*, Vol. 23, No. 1, 1994, pp. 1–22.

[18]Anderson, W. K., Rausch, R. D., and Bonhaus, D. L., "Implicit/Multigrid Algorithm for Incompressible Turbulent Flows on Unstructured Grids," 12th Computational Fluid Dynamics Conference, San Diego, CA, AIAA Paper 95–1740–CP, June 1995.

[19]Nielsen, E. J., *Aerodynamic Design Sensitivities on an Unstructured Mesh Using the Navier-Stokes Equations and a Discrete Adjoint Formulation*, Ph.D. thesis, Virginia Polytechnic Institute and State University, Dec. 1998.

[20]Diskin, B., Thomas, J. L., Nielsen, E. J., Nishikawa, H., and White, J. A., "Comparison of Node-Centered and Cell-Centered Unstructured Finite-Volume Discretizations: Viscous Fluxes," *AIAA Journal*, Vol. 48, No. 7, July 2010, pp. 1326–1338.

[21]Nielsen, E. J., Lu, J., Park, M. A., and Darmofal, D. L., "An Implicit, Exact Dual Adjoint Solution Method for Turbulent Flows on Unstructured Grids," *Computers and Fluids*, Vol. 33, No. 9, 2004, pp. 1131–1155.

[22]Dacles-Mariani, J., Zilliac, G. G., Chow, J. S., and Bradshaw, P., "Numerical/Experimental Study of a Wingtip Vortex in the Near Field," *AIAA Journal*, Vol. 33, No. 9, Sept. 1995, pp. 1561–1568.

[23]Nielsen, E. J. and Anderson, W. K., "Recent Improvements in Aerodynamic Design Optimization on Unstructured Meshes," *AIAA Journal*, Vol. 40, No. 6, 2002, pp. 1155–1163.

[24]Park, M. A., *Anisotropic Output-Based Adaptation with Tetrahedral Cut Cells for Compressible Flows*, Ph.D. thesis, Massachusetts Institute of Technology, Sept. 2008.

[25]Eisenstat, S. C., Elman, H. C., and Schultz, M. H., "Variational Iterative Methods for Nonsymmetric Systems of Linear Equations," *SIAM Journal on Numerical Analysis*, Vol. 20, No. 2, April 1983, pp. 345–357.

[26]Venditti, D. A., *Grid Adaptation for Functional Outputs of Compressible Flow Simulations*, Ph.D. thesis, Massachusetts Institute of Technology, June 2002.

[27]Park, M. A., "Three–Dimensional Turbulent RANS Adjoint–Based Error Correction," AIAA Paper 2003–3849, June 2003.

[28]Lee-Rausch, E. M., Park, M. A., Jones, W. T., Hammond, D. P., and Nielsen, E. J., "Application of a Parallel Adjoint-Based Error Estimation and Anisotropic Grid Adaptation for Three-Dimensional Aerospace Configurations," AIAA Paper 2005–4842, June 2005.

[29]Park, M. A., Lee-Rausch, E. M., and Rumsey, C. L., "FUN3D and CFL3D Computations for the First High Lift Prediction Workshop," AIAA Paper 2011-0936, Jan. 2011.

[30]Alauzet, F. and Loseille, A., "High-Order Sonic Boom Modeling Based on Adaptive Methods," *Journal of Computational Physics*, Vol. 229, No. 3, Feb. 2010, pp. 561–593.

[31]Park, M. A. and Darmofal, D., "Parallel Anisotropic Tetrahedral Adaptation," AIAA Paper 2008–917, Jan. 2008.

[32]Andren, J. and Park, M. A., "Output Based Grid Adaptation for Viscous Flow," 18th International Meshing Roundtable Research Notes, Sandia National Lab, Oct. 2009, pp. 1–5.

[33]Park, M. A. and Carlson, J.-R., "Turbulent Output-Based Anisotropic Adaptation," AIAA Paper 2010–168, Jan. 2010.

[34]Rudnik, R., Huber, K., and Melber-Wilkending, S., "EUROLIFT Test Case Description for the 2nd High Lift Prediction Workshop," AIAA Paper 2012-2924, June 2012.

[35]Rumsey, C. L. and Lee-Rausch, E. M., "NASA Trapezoidal Wing Computations Including Transition and Advanced Turbulence Modeling," AIAA Paper 2014-0747, June 2012.